J. Fluid Mech. (1999), *vol.* 379, *pp.* 191–222. Printed in the United Kingdom

Gentle spilling breakers: crest profile evolution

By JAMES H. DUNCAN[1], HAIBING QIAO[1], VASANTH PHILOMIN[1] AND ALEXANDRA WENZ[2]

[1]Department of Mechanical Engineering, University of Maryland, College Park, MD 20742, USA

[2]Lehrstuhl A für Thermodynamik, Technische Universität München, Boltzmannstr 15, 85748 Garching, Germany

(Received 24 July 1997 and in revised form 25 May 1998)

The surface profile histories of gentle spilling breakers generated mechanically with a dispersive focusing technique are studied experimentally. Froude-scaled generation conditions are used to produce waves with three average frequencies: $f_0 = 1.42$, 1.26, and 1.15 Hz. At each frequency, the strength of the breaker is varied by varying the overall amplitude of the wavemaker motion. It is found that in all cases the beginning of the breaking process is marked by the formation of a bulge in the profile at the crest on the forward face of the wave. The leading edge of this bulge is called the toe. As the breaking process continues, the bulge becomes more pronounced while the toe remains in nearly a fixed position relative to the crest. Capillary waves form ahead of the toe. At a time of about $0.1/f_0$ after the bulge first becomes visible, the toe begins to move down the face of the wave and very quickly accelerates to a constant velocity which scales with the wave crest speed. During this phase of the breaker evolution, the surface profile between the toe and the crest develops ripples which eventually are left behind the wave crest. It is found that the height of the toe above the mean water level scales with the nominal wavelength $\lambda_0 = g/(2\pi f_0^2)$ of the breaker, while the size and shape of the bulge and the length of the capillary waves ahead of the toe are independent of f_0.

1. Introduction

The formation of plunging breakers is well known to casual observers of the ocean surface. As these waves steepen, a jet forms on the front face. This jet falls forward and impacts with the free surface ahead of the crest; a turbulent flow ensues, dissipating the energy of the wave motion and entrapping air in the underlying flow. The formation of spilling breakers, particularly those of short wavelength, is not as well known. As seen by the casual observer, a small turbulent patch rather suddenly appears at the crest on the forward face of the wave as it steepens. The leading edge of this turbulent patch moves down the wave face, much like a snow avalanche on a mountainside. The origination of the small turbulent patch at the crest occurs too rapidly to be observed by the unaided human eye.

Experimental observations of wind-generated short-wavelength spilling breakers in wave tanks have been reported by Okuda (1982) and Ebuchi, Kawamura & Toba (1987). Okuda (1982) used flow visualization techniques to examine the velocity field in 10 cm long waves generated at wind speeds of about 6 m s^{-1}. A region of high vorticity was found in the crest. Ebuchi *et al.* (1987) used specular reflection and side view photographs to study the water surface shape for experimental conditions

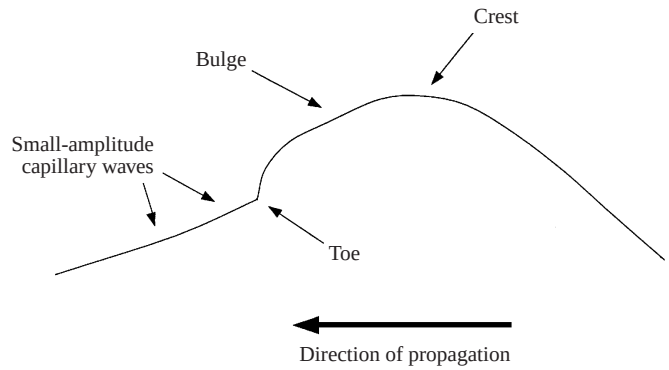

FIGURE 1. Schematic of early stage of breaker formation (from Duncan *et al.* 1994*b*).

similar to those used by Okuda (1982). The photographs show a bore-like structure with a well defined leading (leeward) edge (toe). Capillary waves were found on the leeward side of the toe (see figure 11 of Ebuchi *et al.* 1987). In an earlier study of the shape of wind-generated capillary waves, Schooley (1958) observed photographically wind wave shapes (wavelengths $\approx$ 8 cm, see figure 9 of Schooley 1958) similar to those found by Ebuchi *et al.* (1987). The flow observed by Okuda (1982) and Ebuchi *et al.* (1987) was examined theoretically by Longuet-Higgins (1992). In this theory, it is shown that the capillary waves upstream of the toe generate vorticity and it is theorized that this vorticity is convected into the crest region. The theory provides a plausible explanation of the experimental observations. The theory does not consider the surface stress induced by the wind but it is argued that this stress is not nearly as strong as the effective stress induced by the capillary waves.

Experimental studies of mechanically generated spilling breakers are relatively rare. Bonmarin (1989) measured geometrical parameters describing the evolution of both plunging and spilling breakers with frequencies ranging from about 1 to 2 Hz. This study concentrated on the evolution of symmetry factors describing the overall shape of the waves and on the surface motions induced by the jet impact in the plunging breakers; no crest profiles similar to those observed by Ebuchi *et al.* (1987) were discussed. Recently, Duncan *et al.* (1994*a,b*) presented photographs of the evolution of spilling breakers. These waves were produced mechanically by a dispersive focusing method which was used extensively by Rapp & Melville (1990); however, in Duncan *et al.* (1994*a,b*) the amplitude of the wavemaker motion was reduced until the breaking was extremely weak. The average frequency of the wave packet used to create the breakers was 1.42 Hz (f_0) which by linear wave theory would indicate a wavelength of 77.43 cm. It was found that as the wave steepened a 'bulge' formed on the forward face at the crest (see figure 1 of the present paper). The leading edge of this bulge, called the toe, remained fairly stationary relative to the crest as the bulge grew in amplitude. Concurrent with the growth of the bulge, capillary waves appeared and grew in amplitude upstream of the toe. After a short time, the toe began a rapid motion down the wave face and during this motion a train of large-amplitude well organized ripples formed between the toe and the crest. These ripples grew rapidly and then broke down into a random pattern indicating that the underlying flow had become turbulent. The process from the first appearance of the bulge to the fully turbulent flow took about 0.13 s, or $0.19T_0$ where $T_0 = 1/f_0$.

Theoretical work, complementary to the observations of Duncan *et al.* (1994*a,b*) has been presented by Longuet-Higgins and his co-authors (see Longuet-Higgins 1996*a*). One aspect of this work concerns crest instabilities of the almost highest Stokes wave. In Longuet-Higgins & Cleaver (1994) and Longuet-Higgins *et al.* (1994), it was shown that this instability manifests itself in the form of a bulge shape at the crest on the forward face of the wave with a point of high upward surface curvature at its leading edge or toe. This finding is in qualitative agreement with the experimental findings of Duncan *et al.* (1994*a,b*). The horizontal position of the toe was found to be $0.45R$ ahead of the crest, where R is the radius of curvature of the undisturbed wave crest. In Longuet-Higgins & Dommermuth (1997), the nonlinear development of the fastest-growing crest instability was calculated by using a boundary-integral time-stepping numerical method. It was found that the previously calculated unstable mode leads to a plunging breaker. None of the above theoretical studies include surface-tension effects, thus the capillary waves found in the experiments were not computed.

In an attempt to model the capillary phenomena found in these breakers, a 'capillary jump' theory was presented in Longuet-Higgins (1996*b*). The capillary jump consists of two half solitary capillary-gravity waves. The point of the minimum surface height where the two half-waves are joined would be equivalent to the toe in the unsteady breakers. The capillary jump can be 'leaky' or 'trapped'. In the 'leaky' case, a train of capillary waves is found in front of the jump as observed in the experiments of Duncan *et al.* (1994*a,b*). The theory considers the flow to be steady and the amplitude and phase speed of the underlying gravity wave must be such that there is a region of the crest where the surface flow speed in the reference frame of the crest is less than the minimum phase speed for linear capillary-gravity waves.

The effect of surface tension on breakers was also explored through numerical simulations in several studies. A potential-flow boundary-element method was used by Yao (Yao, Wang & Tulin 1996 and Longuet-Higgins 1996*b*) as a numerical wave tank to simulate the experiments of Duncan *et al.* (1994*a,b*). The computed surface shapes were very similar to those observed experimentally. A study of breakers generated by the modulation of a wave train due to sideband instabilities has been presented by Tulin (1996) using the same computer code as Yao *et al.* (1996). For wavelengths below about 50 cm, crest profiles similar to those reported by Duncan *et al.* (1994*a,b*) were found. As the wavelength was increased above 50 cm, the breaker gradually transformed such that a small jet appeared at the crest, indicating that longer spilling breakers are initiated by a small plunging event. The effect of surface tension on the nonlinear development of the crest instability of the almost highest wave was described in Longuet-Higgins (1996*a*). A boundary-element numerical simulation was used (performed by D. Dommermuth). Calculations were shown for wavelengths of 132 cm and 16.7 cm, both of which showed crest profiles that are qualitatively similar to those found in Duncan *et al.* (1994*a,b*). The above-described numerical simulations indicate that the formation of the bulge, toe and capillary waves is dominated by surface tension forces and that these surface structures occur for breakers generated by both the dispersive focusing (for weak breakers) and sideband instability methods and those that evolve from crest instabilities of the almost highest wave. It should be noted, however, that the critical wavelength below which these crest structures occur and perhaps the details of the crest shape may also depend on the breaker generation method.

The longer ripples generated between the toe and the crest as the toe moves down the wave face (Duncan *et al.* 1994*a,b*) were addressed theoretically in Longuet-Higgins

(1994). The theory assumes that these ripples are the result of shear-flow instabilities arising from the vorticity shed by the capillary waves upstream of the toe. While it seems likely that these ripples are the manifestation of an instability of a shear layer, Duncan *et al.* (1994*a*), taking note of the fact that the ripples do not appear until after the toe motion begins, assumed that the shear layer was generated between a gravity-induced downslope flow near the surface and the underlying upslope flow.

As can be seen from the above discussion, experimental data on the evolution of the profile of gentle spilling breakers are relatively scarce. Also, though the theoretical and numerical work cited above has elucidated some of the dynamic processes in spilling breakers, detailed comparisons of this work with experimental data have not been presented (other than the work of Yao *et al.* 1996) and the theory/numerical work is limited to times in the wave evolution before the transition to a turbulent flow. The goals of the present experimental research programme are to explore the dynamics of gentle spilling breakers over the entire breaking process and to provide detailed surface profile data for use in future theoretical or numerical investigations. To this end, spilling breakers generated by dispersive focusing with wavelengths of about 1 m are investigated quantitatively via crest profile history measurements. These measurements are obtained from individual frames of high-speed movies taken in a reference frame moving with the wave crest. Three average wave packet frequencies and several overall wavemaker motion amplitudes were used to create a total of eight different experimental conditions. A number of the conditions are Froude scaled to all three frequencies in order to explore the combined effects of surface tension and viscosity on the breakers. Great care was taken to control and measure the presence of naturally occurring surfactants as manifested by the *in situ* surface tension. To this end, the water surface was skimmed continuously during the experiments and an *in situ* Langmuir trough was used to monitor the surface tension isotherm. In all the wave measurements reported herein, the surface tension was equal to that of pure water even when the surface was compressed to one fourth of its initial area.

The remainder of this paper is divided into five sections. The experimental setup and measurement techniques are presented in §2. The results of the measurements for a single experimental condition are then presented in §3 and the results for the various waves are compared in §4. These results are discussed in §5. Finally, the conclusions are given in §6.

2. Experimental details

2.1. *The wave tank*

The experiments were performed in a tank that is 14.8 m long, 1.22 m wide and 1.0 m deep (see figure 2). The waves were generated mechanically by a vertically oscillating wedge which spans the width of the tank at one end. The side of the wedge closest to the endwall of the tank is vertical and the opposite side of the wedge is inclined at an angle of 30° from vertical. The wavemaker is driven by a ball-screw and linear-bearing mechanism that is in turn driven by a servo-motor. A computer-based feedback control system is used with a position sensor and a tachometer to provide precise control of the motion of the wedge. Repeated tests with the same wavemaker input parameters indicate only a $\pm 0.1\%$ root-mean-square error in wedge position at the time of peak displacement from the mean water level. An instrument carriage that is driven by a towing wire and a separate servo motor travels above the tank. The carriage is supported by four hydrostatic oil bearings which ride on a pair of

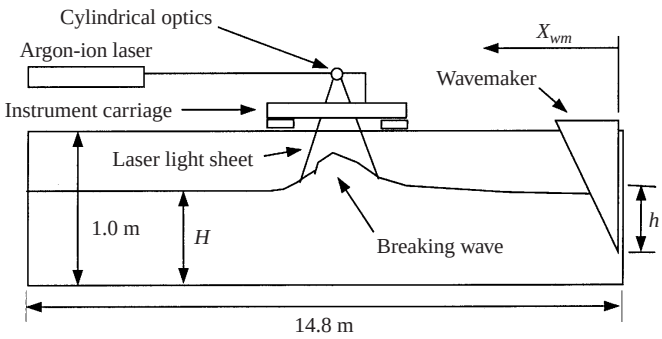

FIGURE 2. Schematic showing tank, wavemaker and carriage.

precision rails positioned one on each side of the tank. This bearing system provides a very low vibration level. The carriage is controlled by the same computer that controls the wavemaker. A position sensor that is connected to the computer is used to control the starting position of the carriage while the velocity of the carriage is controlled via a motor tachometer.

2.2. *Wave generation method*

The breaking waves were generated by a method similar to that described in Rapp & Melville (1990). In this method, a packet of waves with varying frequency is generated in a manner such that the packet converges as it travels along the tank. This convergence causes the amplitudes of the remaining waves in the packet to increase. Eventually a breaking wave is formed if the initial wave amplitudes are large enough. Linear deep-water wave theory is used to compute a suitable motion for the wavemaker though the resulting wave motion is highly nonlinear when the packet converges. The wave packet consists of the sum of N sinusoidal components and the wavemaker motion to produce these waves is given by

$$z_w = w(t)\frac{2\pi}{N}A\sum_{i=1}^{N}\frac{1}{k_i}\cos\left(x_b\left(\frac{\omega_i}{\bar{c}}-k_i\right)-\omega_i t+\frac{\pi}{2}\right), \tag{2.1}$$

where w is a window function which is described below, A is an adjustable constant called the wavemaker amplitude, x_b is the horizontal position of the breaking event (by linear theory) measured from the back of the wedge (for purposes of the experiment), t is time, k_i and ω_i are, respectively, the wavenumber, and frequency of each of the $i = 1$ to N wave components ($\omega = 2\pi f$ where f is the frequency in cycles per second), and $\bar{c}$ is the average of the group velocities ($c_i = 0.5\omega_i/k_i$) of the N components. The frequencies are equally spaced, $\omega_{i+1} = \omega_i + \Delta\omega$, where $\Delta\omega$ is a constant. The window function was chosen to give the wedge zero motion at times when the summation of components resulted in only a very small motion:

$$w(t) = 0.25(\tanh(\beta\bar{\omega}(t-t_1))+1)(1-\tanh(\beta\bar{\omega}(t-t_2))), \tag{2.2}$$

where β is a constant that determines the rise rate of the window function, chosen as 5.0, and $\bar{\omega}$ is the average of the N frequencies ω_i. The window function is nearly equal to 1.0 for most of the time between $t = t_1$ and $t = t_2$ and is zero at other times. The times t_1 and t_2 were chosen to allow the lowest and highest frequency components ($i = 1$ and $i = N$, respectively) to be generated and to travel to position x_b:

$$t_1 = x_b\left(1/\bar{c} - 1/c_N\right), \tag{2.3}$$

f_0 (Hz)	λ_0 (cm)	$A\|_1/\lambda_0$	$A\|_2/\lambda_0$	$A\|_3/\lambda_0$	U (cm s^{-1})
1.42	77.43	0.0487	0.0496	0.0505	94.5
1.26	98.34	0.0492	0.0496	0.0505	102.1
1.15	118.06	—	0.0496	0.0505	112.8

TABLE 1. Wave generation parameters.

$$t_2 = x_b \left(1/\bar{c} - 1/c_1\right). \tag{2.4}$$

Eight different spilling breakers were studied in the present experiments. For all of these breakers, $N = 32$, $h/\lambda_0 = 0.35792$ (where h is the vertical distance between the mean water level and the vertex of the wedge and $\lambda_0 = 2\pi g/\bar{\omega}^2$, where g is gravitational acceleration), $H/\lambda_0 = 0.7458$ (H is the mean water depth in the tank), $x_b/\lambda_0 = 6.0$, and $N\Delta\omega/\bar{\omega} = 0.666$. The eight breakers were generated with three average frequencies ($f_0 = \bar{\omega}/2\pi = 1.42$, 1.26 and 1.15 Hz) and several values of dimensionless wavemaker amplitude (A/λ_0, see table 1). At the smallest A/λ_0 for each frequency, the wave breaking was the weakest possible. These weakest breakers were selected by varying the wavemaker amplitude in steps of $0.0001\lambda_0$ and observing the resulting waves; the weakest breaker at each frequency was taken as the one with the lowest A/λ_0 for which the wave would break every time the wave was produced. As can be seen from the table, A/λ_0 for the weakest breaker increased as the frequency decreased. Increasing A/λ_0 above the minimum values at each frequency increased the apparent breaker intensity. While it seems that the percentage change in A for each frequency is small, observations indicated a considerable variation in apparent breaking intensity. Also, values of A/λ_0 larger than those in the table caused different wave crests to break at positions closer to the wavemaker. (With sufficient wavemaker amplitude, these waves plunge during the breaking process.) As can be seen from the table, the two higher values of A/λ_0 (0.0496 and 0.0505) were repeated for all three values of f_0. Thus, for these two values of A/λ_0 the wave generation parameter sets at the three different frequencies are Froude scaled. Accuracy tests of the resulting wavemaker motions indicate that the dimensionless peak wedge displacements, z_w/λ_0, for the three values of f_0 at identical values of A/λ_0 were the same to within $\pm 0.2\%$ r.m.s.

2.3. *Water surface characteristics*

During preliminary measurements, it was found that gentle spilling breakers are strongly affected by ambient surfactants found in the wave tank under normal operating conditions. In order to perform well controlled repeatable experiments, it was therefore necessary to measure and control the level of ambient surfactants. The surfactant level was monitored by measuring the surface pressure isotherm with a Whilhelmy plate device in combination with an *in situ* Langmuir trough (see figure 3). The Whilhelmy Plate was made of a thin platinum film measuring 0.08 mm in thickness, 28.7 mm in width and about 40 mm in height. The surface of the platinum film was roughened with an emery cloth. The film was then attached to a thin wire bridle which was in turn attached to an under-hook on an electronic balance (FX-40, manufactured by AND). The balance has an accuracy of 0.1 mg. This device was then mounted on a frame which was in turn mounted on a linear traverser so that the entire device could be moved vertically relative to the wave tank. The Langmuir trough was created from a Plexiglas tube that was 46 cm in diameter

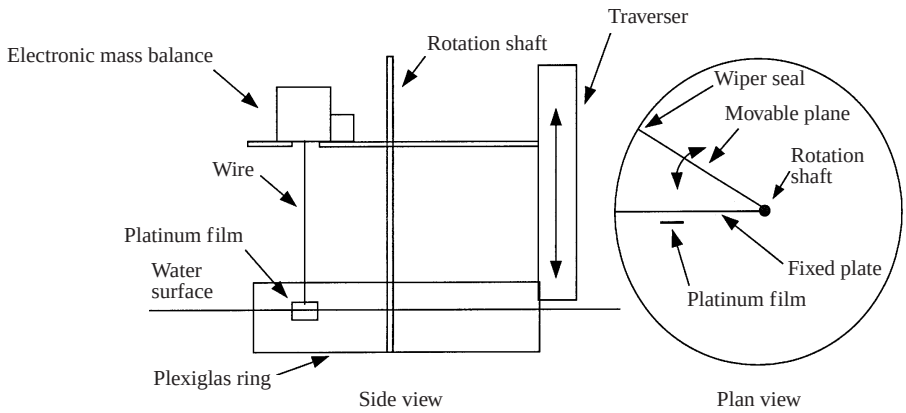

FIGURE 3. Schematic showing Whilhelmy plate and Langmuir trough.

and about 20 cm long. A stainless steel plate with length equal to the inner radius of the Plexiglas tube and height about equal to the length of the tube was fixed to the tube as shown in figure 3. A second plate of equal size was attached to a drive shaft mounted in the centre of the Plexiglas tube. The Plexiglas tube and the two stainless steel plates were coated with paraffin to create a non-wetting surface. A flexible Teflon seal was used to connect the fixed plate to the rotation shaft. A Teflon wiper was used to form a seal between the movable plate and the Plexiglas tube. This entire device was attached to the traverser along with the electronic balance and Whilhelmy plate and the traverser was attached to a platform built over the tank near the wavemaker. At the beginning of each measurement, in order to remove any material on the Platinum film, it was heated with a propane torch until it glowed red. After the film cooled, the balance was zeroed and the device was lowered into the water until the Plexiglas tube, the stainless steel plates and the platinum film were all partially submerged to a depth of about 1 cm. When the platinum film reached the water, the surface tension of the water pulled down on the film and the force as measured by the balance divided by the wetted perimeter of the platinum film gave the surface tension. Each measurement was started with the stainless steel plates nearly touching and the platinum film on the opposite side of the fixed plate from the movable plate. The surfactants were then compressed by turning the shaft and the surface tension as a function of the compressed water surface area was recorded. These data then yielded the surface tension isotherm. Measurements such as this were taken before and after each series of five or six breaker experimental runs.

The surfactant level in the tank was controlled with a skimmer system in which new water was pumped into the bottom of the tank at the end near the wavemaker and old water was removed through two surface skimmers at the end of the tank farthest from the wavemaker. In most cases, using untreated tap water, it was possible to make the water clean enough (as defined below), but some times it was necessary to ozonate the tap water before it entered the tank. In any case, before each series of wave measurements was made, the skimmer system was turned on for about four hours and the surface pressure isotherm was measured periodically. Wave measurements were only made when the measured surface tension without surface compression was close to the accepted value for pure water (about 72 dyne cm^{-1}) and when compression of the surface by a factor of four produced only slight changes in the measured surface tension. Typical curves of the surface tension versus surface area

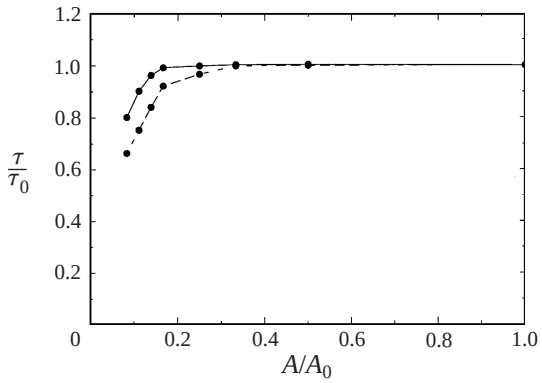

FIGURE 4. Typical measurements of surface tension (τ) versus surface area (A) in the Langmuir trough. In this plot, τ_0 is the surface tension measured without surface compression and A_0 is the initial uncompressed area of the water surface in the Langmuir trough. The solid curve was measured before a series of wave measurements. The dotted curve was measured after the wave measurements.

from before and after a set of wave measurements are shown in figure 4. It should be noted that the curves before and after the wave measurements are not equal. Before the wave measurements, the tank reaches a stable state and the surface tension versus area curves do not change appreciably with time. However, during the wave experiments, the flow into the skimmers is disturbed and the surfactant level increases, thus producing a lower surface tension at the same surface area compression.

2.4. *High-speed movies*

All of the wave profile measurements reported herein were obtained from individual frames of high-speed movies. The movies were taken with a 16 mm camera (Photec 4, manufactured by Photographic Analysis, Inc.) operating at a nominal frame rate of 500 per second. The camera was mounted on the instrument carriage and viewed the wave from the side looking down from above the water surface with an angle of about 5° from the horizontal, see figure 5. (The distortion of the wave profile due to the small angle between the line of sight of the camera and the normal to the light sheet was explored by photographing targets of known geometry. The resulting distortion was deemed negligible.) At the centre plane of the tank, the field of view of the camera was about 12 cm in the horizontal. Kodak SO-078 negative movie film (800 ASA) was used. An argon ion laser was mounted on the wave tank at the end opposite from the wavemaker and was adjusted such that the beam was parallel to the water surface and in the direction along the mid-plane of the tank (see figure 2). The light beam was converted into a light sheet oriented along the centre vertical plane of the tank by a polygonal mirror with 12 facets which rotated at 25 000 r.p.m. and was mounted on the instrument carriage (see figures 2 and 5). The thickness of the light sheet was adjusted to about 1 mm at the mean water surface by two cylindrical lenses that were also mounted on the carriage.

Fluorescein dye was mixed with the water to a concentration of about 2–3 p.p.m. The dye illuminated by the light sheet glowed and formed the light source for the photographs. Two light-emitting diodes were mounted on the carriage just behind the light sheet and positioned such that they appeared in the upper right and left corners of each image. The diodes were nearly at the same height above the water surface and separated by 10.22 cm in the horizontal. During the subsequent image processing,

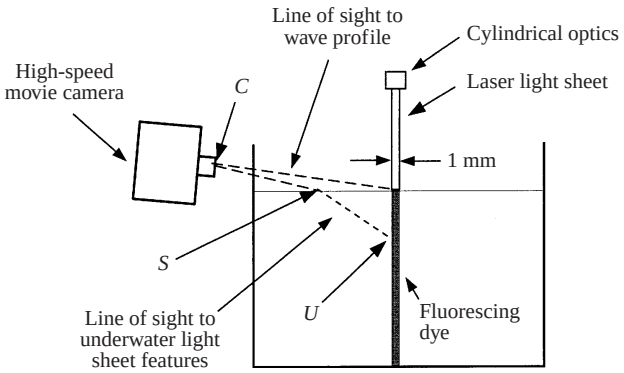

FIGURE 5. Schematic showing end view of tank with light sheet and fluorescing dye.

the images of these diodes were used to align successive frames of the film. By trial and error, the speed, starting position, and starting time of the carriage were adjusted to make the camera view the breaking wave in a reference frame nearly fixed with respect to the wave crest, which was illuminated by the laser light sheet.

The final carriage speeds (crest speeds) are listed in table 1 and are given the symbol U. The frame rate and carriage speed were checked from the high-speed movies. To this end a piece of aluminium plate was mounted to the tank in such a way that it blocked the light going from the LEDs to the camera as the carriage passed by. The camera also puts a light mark on the film every 0.01 s. With the known distance between the LEDs and the measured frame rate of the camera it was possible to calculate the carriage speed and compare it to the value measured directly from the carriage motion with the aid of a stop watch. It was found that the frame rate was actually about 472 per second and that it was still increasing slightly at the time the wave images were taken. Thus, the time between frames is known to an accuracy of about $\pm 1\%$.

2.5. *Measurements*

All measurements presented in this paper were taken from individual frames of the high-speed movies described above. Sample photographs from one of the movies are shown in figures 6–11. (The wave motion shown in the figures will be discussed later in this paper.) The upper edge of the wavy light region between the upper and lower dark regions in each photograph is the wave crest profile at the centreline of the tank where the laser light sheet intersects the water surface. The methods used to obtain this wave crest profile from each image are described briefly in §2.5.1. The light region (foreground) below this edge is an image of the glowing dye in the light sheet. The intensity of the foreground varies for two reasons. First, the intensity of the light emitted by the dye varies due to focusing of the light sheet by the curved shape of the water surface where the light sheet enters the water. Second, this non-uniform light intensity pattern is viewed through the curved water surface between the camera and the glowing dye (see figure 5). Thus, the light patterns in the foreground must be interpreted carefully. In §2.5.2, a method is described in which this foreground light pattern is used to determine the wavelengths and amplitudes of the capillary waves found on the forward face of the wave, even when the capillary waves are too small in amplitude to be measured directly from the overall wave profile.

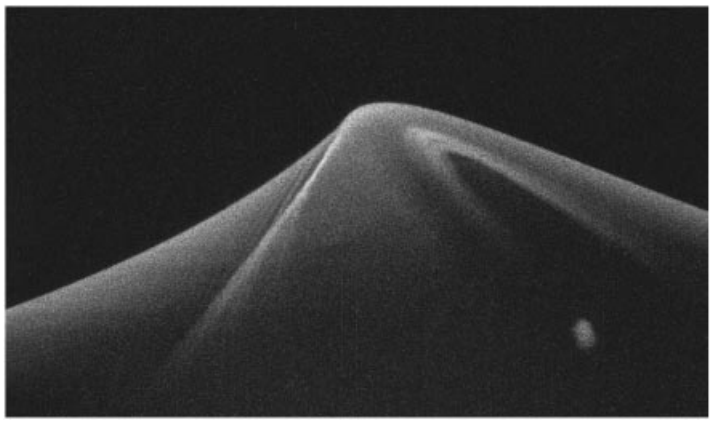

FIGURE 6. Photographs of wave crests from high-speed movie, $f = 1.42$ Hz $A/\lambda_0 = 0.0487$. The horizontal field of view is about 111 mm. The bulge and toe are just beginning to form. $t = 0$.

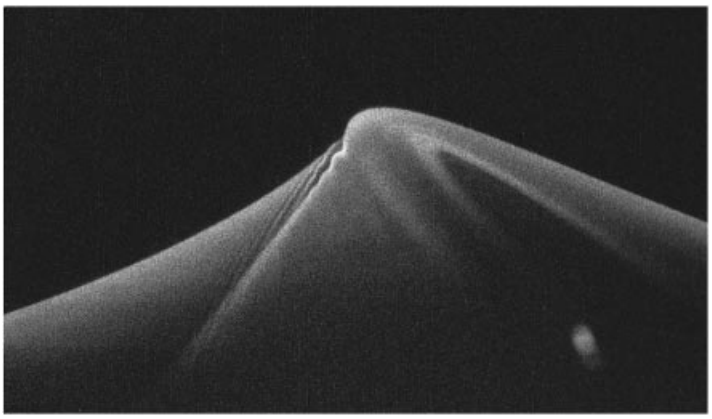

FIGURE 7. As figure 6 but at $t = 0.028$ s. The bulge and toe are well formed. Capillary waves can be seen upstream of the toe.

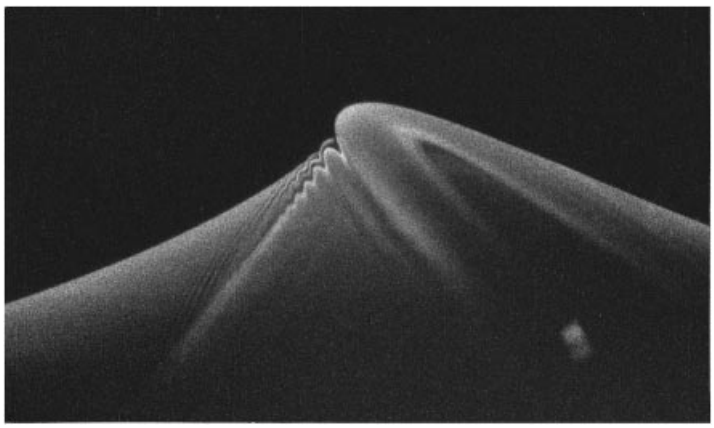

FIGURE 8. As figure 6 but at $t = 0.057$ s. The toe motion is about to start.

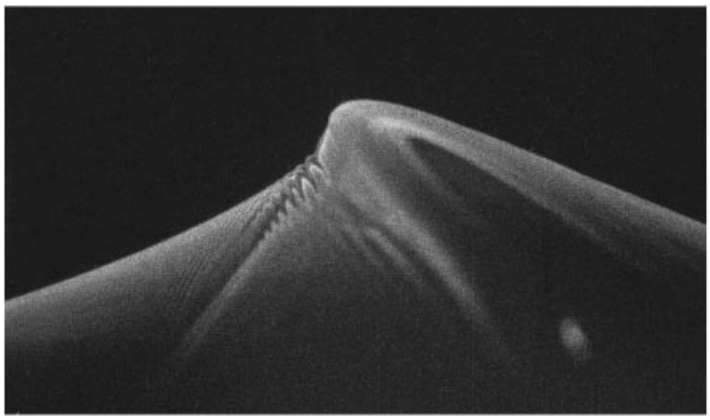

FIGURE 9. As figure 6 but at $t = 0.093$ s. The toe motion has begun.

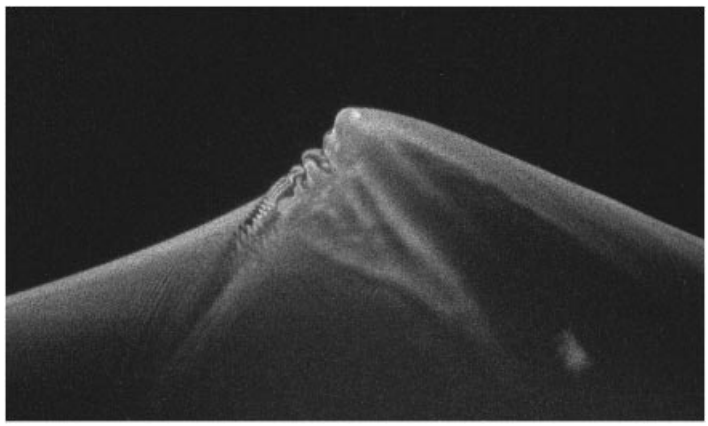

FIGURE 10. As figure 6 but at $t = 0.136$ s. The toe has moved significantly and ripples appear between the toe and the crest.

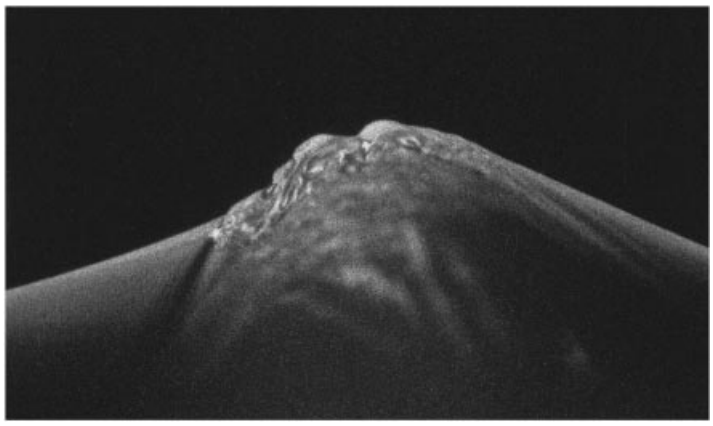

FIGURE 11. As figure 6 but at $t = 0.186$ s. The crest appears to be fully turbulent.

2.5.1. *Extracting the overall wave profile from each image*

Computer based image analysis was used to obtain the wave profile from each image. For this purpose, the images (about 100 per experimental run) were digitized at a resolution of about 1300 by 800 pixels. This resulted in a spatial resolution at the physical plane of the light sheet of about 10 pixels mm^{-1}. The processing of these digitized images to obtain the wave profiles was done in three steps: pre-processing, determination of the LED positions, and determination of the wave profile. These steps are described briefly in the following subsections.

Pre-processing

The wave surface measurements taken from the images are based on the positions of edge contours between the dark background and both the bright alignment LEDs and the glowing dye at the water surface. In order to enhance these edges and reduce the effect of noise on their detection, each image was smoothed first with a symmetric median filter, which removes spot noise, and then with a symmetric neighbourhood filter operator, which flattens the intensity levels in the interior of objects. These pre-processing techniques are described in Harwood *et al.* (1984). After smoothing, the gradient of the image intensity field was obtained via a centred difference in both the x- and y-directions at each pixel, where x and y are Cartesian image coordinates. An edge image was then created from the magnitude of this gradient at each pixel; pixels whose gradient magnitude exceeded some threshold were called edge pixels. The subsequent calculations described below were performed with the resulting edge images as the primary inputs.

Determination of the LED positions

The determination of the positions of the LEDs was difficult because, though the LEDs themselves were round, the images of the LEDs were sometimes irregular in shape due to insufficient light output. The processing to determine the positions of the LEDs starts with an examination of an edge image. For each edge pixel in the general vicinity of either LED, the question is asked: if this pixel is to lie on a circle representing the edge of the LED, what is the locus for the parameters of all the possible circles associated with this edge pixel. These circle parameters are the radius, r, and the row and column coordinates, (a_x, a_y), of its centre. There are two constraints on these parameters. First, the centre of these circles is assumed to lie on the line extending from the edge pixel in the direction given by the local image intensity gradient vector. Second, from observation of the LEDs in the digitized images, the approximate radius of the circle is known. If the set of parameters best representing the LED is defined as $(a_x, a_y, r) = (A_x, A_y, R) = \boldsymbol{A}$, then the parameter spaces of all of the edge pixels that lie on the edge of the LED will pass through, or close to $\boldsymbol{A}$. In order to find $\boldsymbol{A}$, a Hough algorithm was used (see Rosenfeld & Kak 1982; Duda & Hart 1975; Illingworth & Kittler 1987). In this algorithm, an accumulator array $B(a_x, a_y, r)$ which is initially set to zero is used. The accumulator array is set up with bin sizes in each independent variable. Then for each edge pixel, all possible (a_x, a_y, r) as defined above are computed and the corresponding accumulator array bins are incremented by one. Each increment for a particular bin is called a vote. After all edge pixels in the known vicinity of the LED are considered, the bin in the accumulator array with the most votes should correspond to the parameters for the circle that best fits the LED edge pixels. A coarse to fine approach is used by first looking for accumulated votes in coarse bins of the parameter space and then moving on to a finer resolution for those coarse bins with a high accumulation of votes. Many sources of error (Brown 1983) affect the

computation of the parameter vector (a_x, a_y, r) and hence many array locations in the vicinity of the true point $\boldsymbol{A}$ are incremented instead of the point itself. To compensate for these errors, we replace the un-compensated accumulator values with a local weighted averaging of the $3 \times 3 \times 3$ neighbourhood of each bin. This averaging step is followed by a non-maximum suppression to suppress other solutions that are very close to the best solution. Tie values are not suppressed to avoid mutual suppression.

Determination of the wave profile

The crest profiles were located in each image with deformable contour (snake) techniques (see Amini, Weymouth & Jain 1990; Barr 1984; Blake, Curwen & Zisserman 1993; Chakraborty, Woring & Duncan 1995; Delagnes, Benois & Barba 1995; Lai & Chin 1994). Snake techniques are an example of the more general technique of matching a deformable model to an image by means of 'energy' minimization. From any starting point (in the present case the wave profile from the previous image or a manually determined profile in the case of the first image), the snake deforms itself into conformity with the nearest salient edge contour in the image. The snake representation method chosen herein is piecewise Hermite cubic polynomials, Foley *et al.* (1993), which interpolate the intervals between N control points $\boldsymbol{p}_0, \ldots, \boldsymbol{p}_N$ chosen along the snake. In each interval, the Hermite cubic is specified by the positions $\boldsymbol{p}_{i-1}$, $\boldsymbol{p}_i$ and tangent vectors $\boldsymbol{\tau}_{i-1}^{+}$, $\boldsymbol{\tau}_i^{-}$ at the endpoints of each contour segment.

The snake representing the wave profile in a new image was obtained from the snake in the previous image by a two-step procedure: rigid body transformation followed by deformation. In the rigid body transformation step, the previous snake is rotated about its centroid and translated over small displacements in the edge image. For each new position, the sum of the image intensity gradient magnitudes along the new snake is computed. The best rigid body displacement is taken as the one with the maximum total gradient. In the deformation step, the new positions and tangent directions at each control point on the snake are determined sequentially, one segment at a time, starting at one end of the snake. In determining each new control point, its parameters ($\boldsymbol{P}_i = [\boldsymbol{p}_i, \boldsymbol{\tau}_i^{+}, \boldsymbol{\tau}_i^{-}]^T$) are varied by small increments about their starting values. At each test $\boldsymbol{P}_i$, both an internal energy (E_{int}) and an external energy (E_{ext}) are computed. The internal energy measures the difference in shape between the previous and current polynomial and is computed as the sum of the squared distances in $\boldsymbol{P}$-space between the two polynomials. This energy increases as the deformation increases. The external energy is a predetermined large number minus the sum of the gradient magnitudes in the edge image along the new polynomial. The new control point $\boldsymbol{P}_i$ is taken as the one which corresponds to the minimum total energy, $E = 0.1E_{int} + 0.9E_{ext}$, where the relative weighting of E_{int} and E_{ext} was determined by trial and error in order to locate the new polynomial at the maximum gradient without allowing too much deformation from the previous snake. This energy minimization problem was solved using a discrete enumeration technique based on dynamic programming (see Amini *et al.* 1990).

The errors in measuring the full-scale shape of the wave crest involve the errors in determining the positions of the LEDs and surface profiles in the images. It is estimated that lengths and positions can be determined to an accuracy of 1–2 pixels, i.e. 0.1 to 0.2 mm in the physical plane.

2.5.2. *Measuring the capillary waves from each image*

At times in the wave development just before the flow at the crest appears to become turbulent, the first one or two capillary waves found upstream of the toe have

large amplitudes and their shape can be measured directly from the surface profile, as can be seen from figure 8. However, the capillary waves further upstream in figure 8 and all the capillary waves at earlier times in the breaking process (see figures 6 and 7) are too small to measure accurately from the measured surface profile. Therefore, a more sensitive measurement technique was developed. This method is described below.

The capillary wave measurement technique is based on analysis of the light intensity pattern found in the foreground of each image. This light pattern originates from the glowing dye within the light sheet. If one were to look from underwater at the light intensity pattern of the glowing dye, a series of nearly vertical dark and light bands would be visible. Light bands start under regions of the free surface with downward curvature (wave crests) where the incoming light is focused, while dark bands start under regions with upward curvature (wave troughs) where the incoming light is spread out. As the distance downward from the free surface increases, the light intensity decreases and the bands sometimes cross or otherwise interfere with each other. In the high-speed movies, this intensity pattern is viewed from above the water surface with a small look-down angle (about 5°); from this view point, any light reaching the foreground of the images from the glowing dye is refracted by the water surface between the light sheet and the camera (see figure 5). Over most of the width of the tank, the water surface shape is two-dimensional so that the refraction of the light rays reaching the foreground of the image is caused by the same surface shape as is seen at the centre of the tank where the light sheet enters the water. This refraction has two effects on the images of the dark and light bands in the glowing dye. First, though the bands are nearly vertical as seen from underwater, they appear at a much smaller angle to the water surface in the images. Second, the images of the bands have a wavy appearance caused by refraction along the capillary waves where the line of sight from the camera to the underwater features enters the water (see figures 5 and 12). Examples of these image features can be found in figures 6–8. There is a very sharp dark–light boundary (edge) extending from the toe and weaker dark–light rays extending from each capillary wave upstream of the toe. In the present study, an optical theory is presented to obtain the wavelength and amplitude of the capillary waves from the image of the wavy edge extending from the toe (called the toe edge in the following discussion).

In the theory, a light ray coming from the underwater dye that is the source of the toe edge at U in figures 5 and 12 strikes the water surface at S. This ray leaves the water surface at an angle relative to the surface normal as determined by Snells law

$$n_{wa} = \sin\theta_e / \sin\theta_i \tag{2.5}$$

where n_{wa} in the refractive index from water to air, θ_i is the angle between the surface normal at S and the incident light ray $\overline{US}$ and θ_e is the angle between the surface normal and the ray leaving the surface $\overline{SC}$, see figure 12. Of all the rays that leave the toe edge at U, the one that enters the pinhole of the camera after leaving the water surface is the one that appears in the image. Thus, the variation of the surface normal at S due to the two-dimensional capillary waves results in the waviness of the line seen in the foreground of the images. A computer program was written to perform the above described ray analysis. In the program, the toe edge is considered to be straight and the capillary waves are given by the solution due to Crapper (1957):

$$\frac{x}{\lambda} = \alpha - \frac{2}{\pi}\frac{A\sin 2\pi\alpha}{(a + A^2 + 2A\cos 2\pi\alpha)}, \tag{2.6}$$

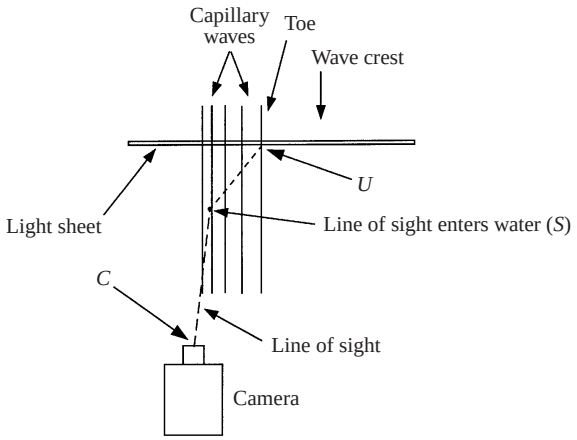

FIGURE 12. Schematic showing plan view of wave with camera, laser light sheet and line of sight to underwater features within the light sheet. See also figure 5.

$$\frac{y}{\lambda} = \frac{2}{\pi} - \frac{2}{\pi}\frac{1 + A\cos 2\pi\alpha}{(a + A^2 + 2A\cos 2\pi\alpha)}, \tag{2.7}$$

where λ is the wavelength,

$$A = \frac{2\lambda}{\pi a}\left[\left(1 + \frac{\pi^2 a^2}{4\lambda^2}\right)^{1/2} - 1\right], \tag{2.8}$$

and a is the amplitude of the wave as measured from the trough to the crest. The above equation is for a uniform wave train while in the present case both the wavelength and the amplitude decrease with distance upstream from the toe. Thus, to better fit the present waveform, λ and a were allowed to vary with distance according to the equations

$$\lambda = \lambda_{first}\frac{1 - b\alpha^{1/2}}{1 - b}, \tag{2.9}$$

$$a = \beta * (1 + \alpha^{1/2})\exp(-\gamma\alpha), \tag{2.10}$$

where λ_{first} is the wavelength of the first capillary wave and b, β and γ are constants that are adjusted to make the equations fit the data. The functional forms of the above two equations were determined to best fit the data by trial and error. The above wave profile was added to a second-order polynomial that was used to represent the mean free surface ahead of the toe. The camera was represented by a pinhole camera with focal length f. The perspective projection equations for this camera are

$$x = fX/Z, \tag{2.11}$$

$$y = fY/Z, \tag{2.12}$$

where x and y are Cartesian image coordinates and X, Y and Z are world coordinates.

To apply the above theory to the images, a program was written in which the capillary wave profile and toe edge profile were computed and plotted as white lines on top of the digitized images from the film. The parameters describing the capillary waves and the slope and intercept of the line representing the toe edge were adjusted by trial and error until the actual and computed images of the rippled toe edge coincided. An example of the results of this analysis can be seen in figure 13 which

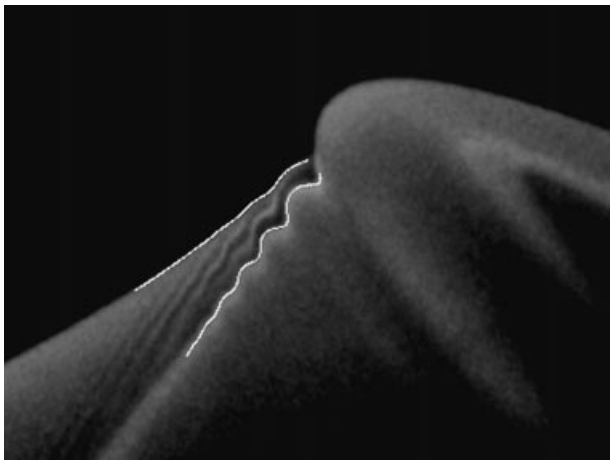

FIGURE 13. Sample digitized image with computed capillary wave profile and corresponding image of toe edge highlighted by white pixels.

contains a digitized version of one of the images from the high-speed movies. Only the region around the wave crest is shown. The calculation results are indicated by the two white lines.

The error in the measurement of the capillary wavelength is estimated to be less than 5% while the error in the capillary wave amplitude is about 8% when the capillary wave is at its maximum amplitude. This estimation is based on tests in which the variation in the capillary wave parameters needed to produce a noticeable mismatch between the calculated toe edge and the real one from the image were determined.

3. Sample results for a single experimental condition

The results for breakers generated with $f_0 = 1.42$ Hz and $A/\lambda_0 = 0.487$ are presented in the following two subsections. These results include sample profile histories of the wave crest and the capillary waves from a single experimental run (§3.1) and histories of various geometrical parameters taken from the profiles for all the runs with the above wave generation parameters (§3.2). The qualitative behaviour described in these subsections is characteristic of all the waves studied herein.

3.1. *Profile histories*

The crest profile history is shown in figure 14. This plot contains profiles from 330 successive images of the wave as it breaks. The total time covered by this image sequence is about equal to the wave period, $1/f_0$. Several of the original images are shown in figures 6–11 and the profiles corresponding to these images are marked in figure 14. For clarity of presentation, a vertical distance $i\Delta$ (where i is the profile number obtained by counting up from the first profile ($i = 0$) at the bottom of the figure and Δ is a constant equal to 1 mm) is added to the height data (measured relative to the undisturbed water surface) for each profile. Thus, for instance, to obtain the actual height of a point on wave profile $i = 100$, one must first read the height from the vertical axis of the plot and then subtract 100 mm. As mentioned above, the profiles are recorded and displayed in a coordinate system fixed with respect to the crest. In these wave-fixed coordinates, the fluid at large depth moves from left to

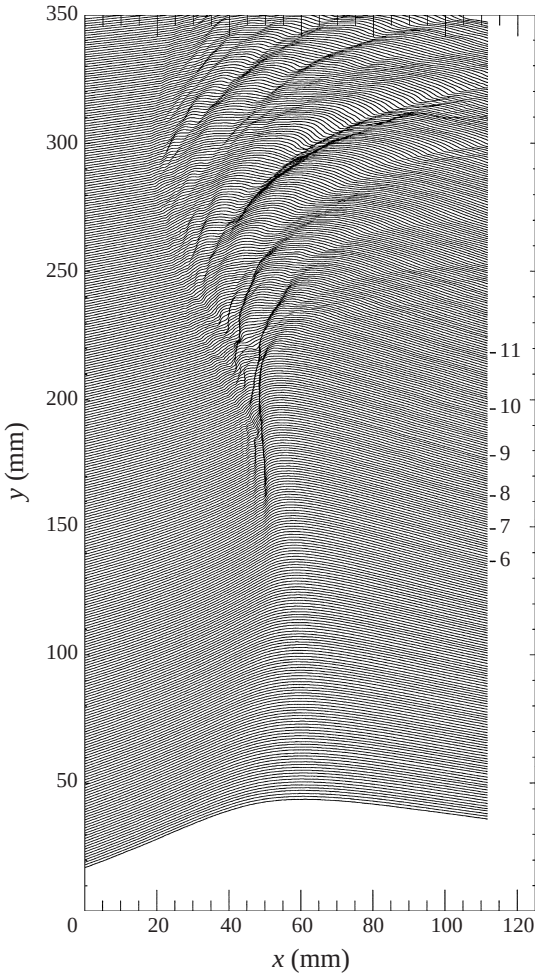

FIGURE 14. Profile history for a single wave ($f = 1.42$ Hz, $A = 0.0487\lambda_0$). Each succesive profile is plotted 1.0 mm above the previous profile for clarity. The profiles are shown in a reference frame fixed with respect to the wave crest. In this reference frame, the mean fluid motion is from left to right. The time between profiles is 2.1 ms. The numbers on the right mark the profiles corresponding to figures 6–11.

right. Thus, in the following descriptions, the upstream direction is defined as toward the left in figure 14 and the forward face of the wave is on the left as well. Profile histories plotted in the above manner are well suited to determining the velocity of profile features (say a crest of a capillary wave) relative to the breaking wave crest since a line connecting the same feature in successive profiles will be vertical if the feature moves with the crest, tilted to the right (positive slope) if the feature moves slower than the crest, or tilted to the left if the feature moves faster than the crest.

As can be seen from figure 14, the breaking process starts with an asymmetric wave profile which is steeper on the front face than on the rear face. After a short time, a bulge develops at the crest on the forward face (see profile marked by 6 and corresponding figure 6, $t = 0$); the upstream edge of the bulge is called the toe (see figure 15). As the process continues, the bulge grows in amplitude while the position of the toe relative to the crest remains fairly constant and capillary waves become

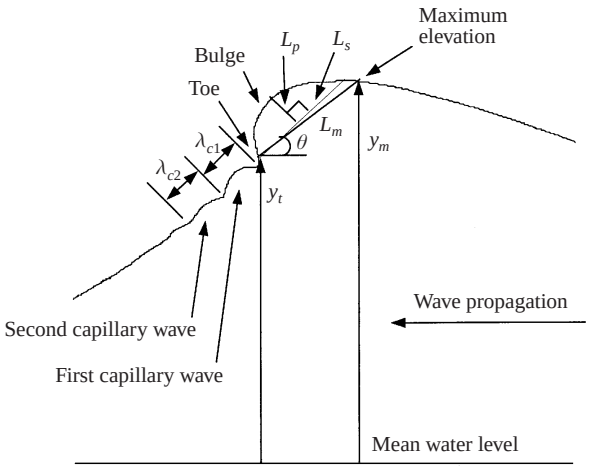

FIGURE 15. Schematic showing nomenclature for breaking wave measurements.

visible upstream of the toe (profiles 7 and 8, $t = 0.028$ s and 0.057 s, respectively). These capillary waves are also stationary relative to the crest. Between profiles 8 and 9 ($t = 0.093$ s), the toe begins to move down the forward face of the wave. As this happens, ripples appear between the toe and the wave crest (profile 10, $t = 0.136$ s). These ripples, which are initially stationary relative to the breaking wave crest, form a relatively random pattern and eventually grow in wavelength and decrease in phase speed so that they are left behind the crest (profile 11, $t = 0.186$ s). The toe eventually reaches a maximum distance from the crest and then begins to retreat.

The corresponding profile history of the capillary waves upstream of the toe is shown in figure 16. The initial amplitude is, of course, quite small. As the amplitudes of the capillary waves increase, the wavelengths decrease. The last profile shown in the figure corresponds to a time just before the toe motion began.

The wave crest evolution in the present experiments is somewhat different from that found in Duncan *et al.* (1994*a*,*b*) even though the wave generation parameters are the same for the present and previous photographs. (Note that for the photographs in Duncan *et al.* (1994*a*) and those in the present paper, the angle between the line of sight of the camera and the mean water surface is about 5° while in Duncan *et al.* (1994*b*) it is about 20°. The main effect of this change in viewing direction concerns the appearance of the foreground of the photographs.) In the present case, the bulge is much rounder and of shorter length (for example compare figure 8 of the present paper with Plate b of Duncan *et al.* 1994*b*). Also, the phase of the breaking just after the toe motion begins, when ripples appear between the toe and the crest (figure 10 in the present paper and Plates c, d and e in Duncan *et al.* 1994*b*), is not as well defined in the present experiments; there are a smaller number of ripples, they last a much shorter time, and they are much less uniform. These differences in wave behaviour are probably due to the differences in surfactant levels between the present and previous experiments. In the previous experiments, the water surface skimming was not carefully controlled and no measurements of surface tension were carried out. However, from experience gained from controlling and monitoring the surface-tension isotherms in the present experiments, it is believed that the surfactant concentration in the previous experiments was high and that the surface tension without surface compression was about 50 dyne cm^{-1}. Experiments to

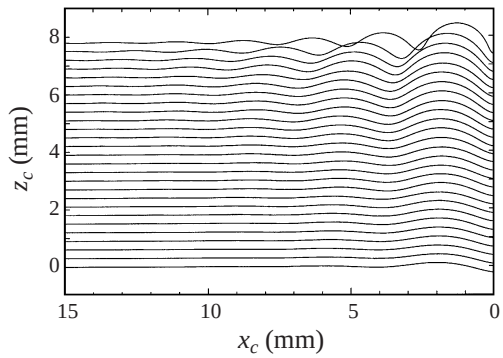

FIGURE 16. Capillary wave profile history for a single wave ($f = 1.42$ Hz, $A = 0.0487\lambda_0$). The profiles are presented in toe fixed coordinates (x_c, z_c) and each succesive profile is plotted 0.3 mm above the previous profile for clarity. The toe is located at $x_c = 0$.

explore quantitatively the effects of surfactants on the breaking process are at present underway in our laboratory.

3.2. *Histories of geometrical parameters*

A number of geometrical parameters, which are defined in figure 15, were obtained from profile histories like those shown in figures 14 and 16. The ten plots in figures 17(*a–e*), and 18(*a–d*) show the results for $f = 1.42$ Hz and $A/\lambda_0 = 0.0487$. Each plot in figure 17 contains data from four experimental runs, while each plot in figure 18 contains data from three experimental runs. The measured parameters are plotted against the distance (X_{wm}) from the back face of the wavemaker to the horizontal position of the crest at the instant each image was recorded by the camera; this distance is non-dimensionalized by λ_0 in the plots. The data points with the smallest X_{wm}/λ_0 correspond to the first frames in the movies where the toe position was discernible. The data points with the largest X_{wm}/λ_0 correspond to about the time when the toe had reached its greatest distance from the crest. It should be noted that the data sets from each run were shifted horizontally in each plot by up to $\pm 0.02 X_{wm}/\lambda_0$ (≈ 2 cm) in order to bring the data from different runs into closer agreement. The necessity for this shifting is primarily a reflection of the fact that the position of the wave along the tank when the toe begins to move down the wave face changes slightly from run to run. This randomness in the starting point of the toe motion is typical of phenomena initiated by an instability. The same shift in X_{wm}/λ_0 was applied to all measured quantities for any particular experimental run. As can be seen from the figures, with the exception of this slight shifting in X_{wm}, the data are quite repeatable. The data shown in these plots are discussed in the following paragraphs.

The histories of the non-dimensional crest height, y_m/λ_0, and toe height, y_t/λ_0, are plotted in figures 17(*a*) and 17(*b*), respectively. The crest height varies smoothly over a small range even through the transition to a turbulent flow which occurs after the toe motion begins. The typical maximum value of y_m/λ_0 from the plot, 0.07, can be compared to the similar quantity, y_{mS}/λ (where y_{mS} is the wave height from mean water level to crest and λ is the wavelength), for a limiting form Stokes wave in deep water. To arrive at a value for y_{mS}/λ one can start with Bernoulli's equation in a reference frame moving with the crest of the Stokes wave. Since the flow speed at the

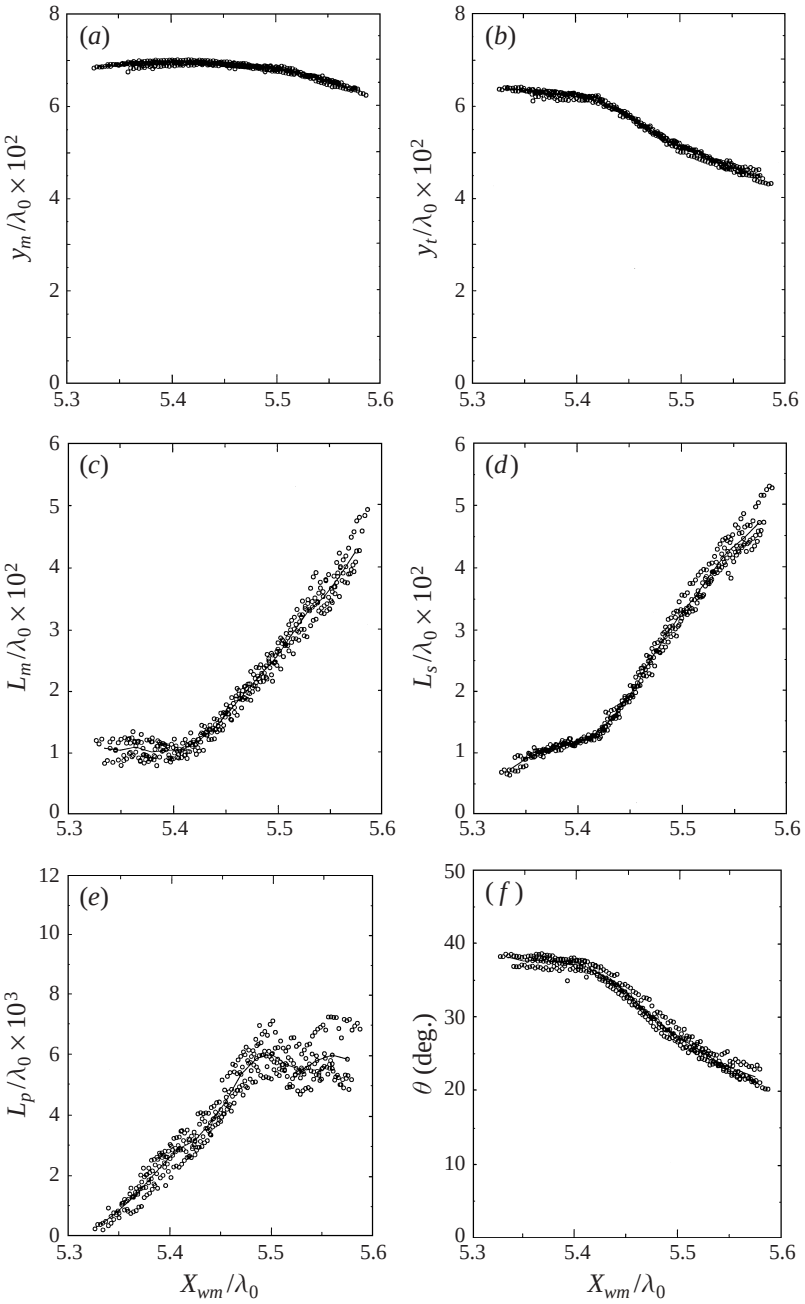

FIGURE 17. Geometrical parameters describing the spilling breaker ($f = 1.42$ Hz, $A = 0.0487\lambda_0$) versus distance (X_{wm}/λ_0) from the wavemaker: (*a*) Crest height, y_m; (*b*) toe height, y_t; (*c*) bulge length from toe to point of maximum height, L_m; and (*d*) bulge length along tangent, L_s; (*e*) bulge thickness, L_p; (*f*) angle (relative to horizontal) of tangent to mean surface just upstream of toe, θ.

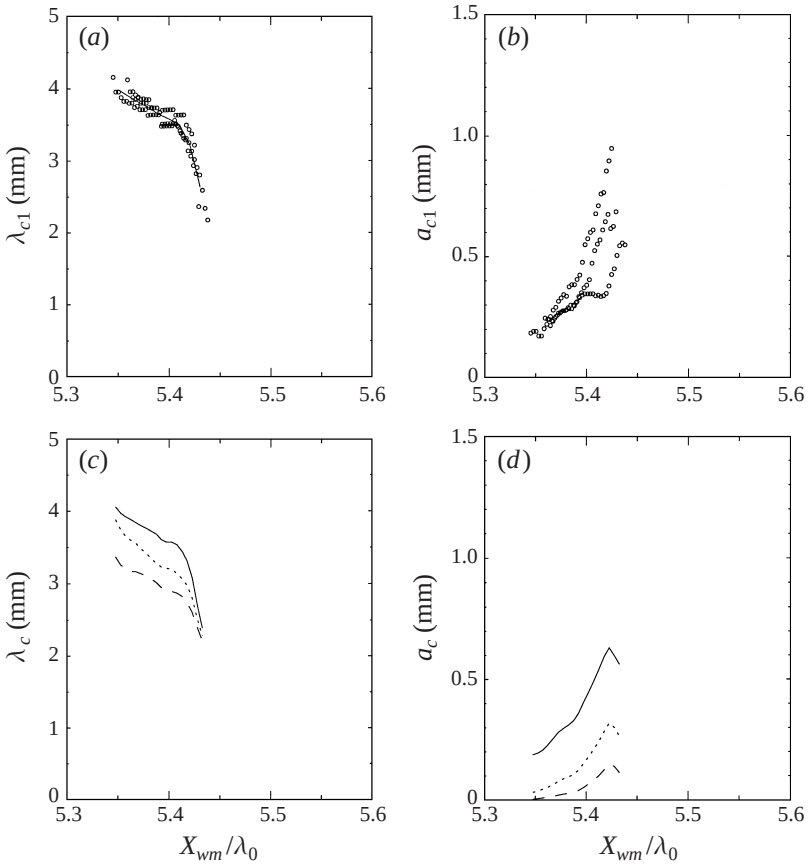

FIGURE 18. Geometrical parameters describing the capillary waves ($f = 1.42$ Hz, $A = 0.0487\lambda_0$): (*a*) wavelength of first capillary wave, λ_{c1}; (*b*) amplitude of first capillary wave, a_{c1}; (*c*) wavelength of first three capillary waves ——— λ_{c1}, · · · · · λ_{c2}, and – – – – λ_{c3}; and (*d*) amplitude of first three capillary waves, ——— a_{c1}, · · · · · a_{c2} and – – – – a_{c3}.

crest is zero in this reference frame, Bernoulli's equation yields

$$y_{mS} = c^2/2g, \tag{3.1}$$

where c is the wave phase speed which was calculated in Longuet-Higgins (1975) to be $1.0923c_0$, where c_0 is the wave speed from linear theory for the given λ. With this result, $y_{mS}/\lambda = 0.0949$, considerably larger than the measured value of y_m/λ_0. In comparing these numbers, it should be kept in mind that the Stokes wave is a steady regular infinitely long wave train with a well defined wavelength, λ, while in the present case the wave is part of an unsteady wave packet of one or two waves and the wavelength, λ_0, is obtained from the average wavemaker frequency via the linear dispersion relation for deep-water waves; no measurements of the overall wavelength were made. The history of the non-dimensional toe height, y_t/λ_0, given in figure 17(*b*) is quite different from that of the crest height. As can be seen from the figure, y_t decreases only slightly in a linear fashion from the point where the toe is initially detected up to about $X_{wm}/\lambda_0 = 5.425$ where the toe motion begins. After this point, y_t decreases more rapidly. The rapid decrease is nearly linear up until about $X_{wm}/\lambda_0 = 5.5$ where the rate begins to slow.

The plots of L_m/λ_0 and L_s/λ_0 in figures 17(*c*) and 17(*d*), respectively, characterize the length of the bulge. As can be seen from the schematic in figure 15, L_m is the length from the toe to the maximum height on the wave profile while L_s is the length from the toe, following the tangent to the mean water surface ahead of the toe, to the wave profile behind the crest. The tangent to the water surface ahead of the toe was obtained by fitting a second-order polynomial to the measured profile in this region. In this way, the capillary waves were effectively averaged out in obtaining the tangent. Note that L_m/λ_0 is initially constant with a value of about 0.01 and then at about $X_{wm}/\lambda_0 = 5.425$ it increases in a nearly linear fashion. On the other hand, L_s/λ_0 increases slowly in a linear fashion at first and then rapidly in a linear fashion after $X_{wm}/\lambda_0 = 5.425$. Note also that the scatter in L_s is considerably less than the scatter in L_m. This is because the top of the wave is nearly flat and therefore the location of the point of maximum y that is used to determine L_m can vary from frame to frame.

Figure 17(*e*) contains a plot of L_p/λ_0, the maximum non-dimensional distance in the direction of the normal from the line L_s to the water surface on the bulge. The data follow a linear curve right through the point where the toe motion begins, $X_{wm}/\lambda_0 = 5.425$. At about $X_{wm}/\lambda_0 = 5.5$, L_p attains a constant value of about $0.006\lambda_0$.

The angle (relative to the horizontal) of the tangent to the mean surface ahead of the toe (as obtained with the second-order polynomial fit as described above) at the location of the toe is plotted in figure 17(*f*). During the time before the toe begins moving down the wave face, this angle is nearly constant with a value of about $\theta = 37.5°$. The corresponding steepest angle found on the face of a limiting form Stokes wave is 30°. Once the toe begins moving, the slope decreases rapidly. It should be kept in mind that, as can be seen from figures 6–8, the wave is asymmetric with the front face much steeper than the rear face.

The length and amplitudes of the capillary waves ahead of the toe are plotted in figures 18(*a–d*). Capillary waves were measured for three of the four experimental runs for this experimental condition. The length (λ_{c1}) and amplitude (a_{c1}) of the first capillary wave ahead of the toe are plotted in figures 18(*a*) and (*b*), respectively, where the individual data points are plotted. The wavelength is initially (the first instance when it is measurable by our optical technique) 4 mm and the amplitude at this point is 0.18 mm. The wavelength decreases linearly to 3.5 mm at $X_{wm}/\lambda_0 = 5.4$ and the amplitude increases to about 0.5 mm. At this point, the wavelength begins to drop off more rapidly, falling to about 2.5 mm when the toe starts to move down the wave face. The maximum recorded wave amplitude in these runs is 1.0 mm. Figures 18(*c*) to 18(*d*) contain plots of the lengths and amplitudes, respectively, of the first three capillary waves ahead of the toe. In these plots, curves obtained by averaging the raw data are presented for clarity of presentation. As can be seen from the data, both the wavelength and amplitude drop off rapidly with distance ahead of the toe. The shapes of the three curves in each plot are quite similar.

4. Comparison of results for different experimental conditions

The behaviour of all the breaking waves is qualitatively similar to that described in the previous section for the breaker with $f = 1.42$ Hz, $A/\lambda_0 = 0.0487$. In the present section, the quantitative similarities and differences between the various waves are presented and discussed with an eye toward elucidating the physical processes that dominate the wave motion. In the interests of brevity, the following discussion will concentrate on the comparison of the weakest breakers (lowest A/λ_0) at each frequency and the comparison of the three breakers with different strengths (different A/λ_0) at

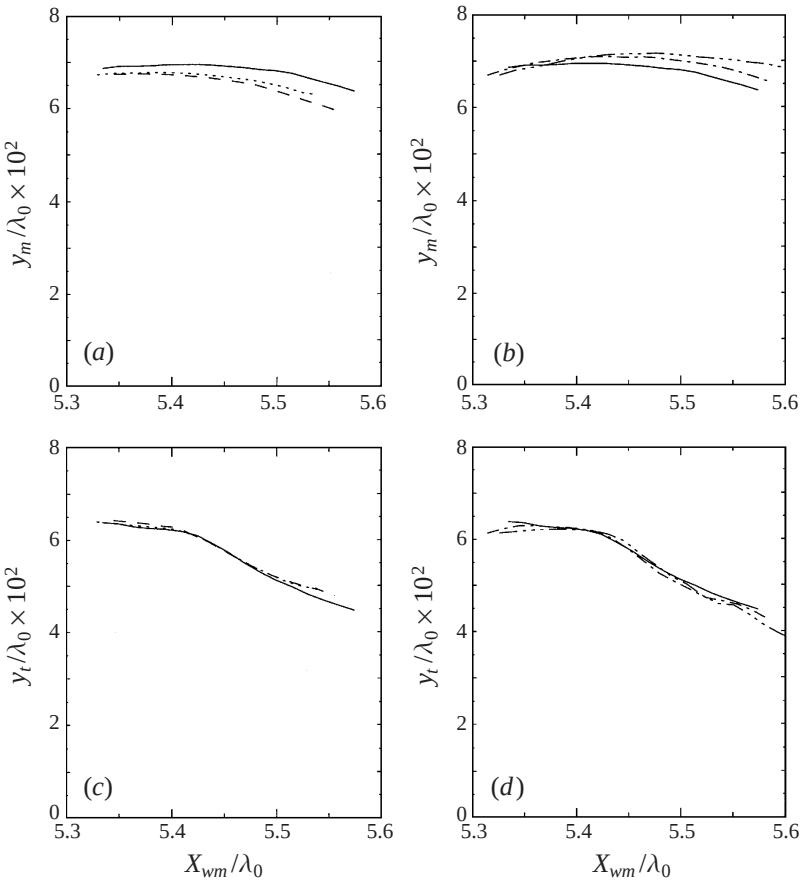

FIGURE 19. Maximum surface height, (*a,b*), and toe height, (*c,d*), versus distance (X_{wm}/λ_0) from the wavemaker: (*a*) and (*c*) ——— $f = 1.42$ Hz, $A = 0.0487\lambda_0$; · · · · · $f = 1.26$ Hz, $A = 0.0492\lambda_0$; – – – – $f = 1.15$ Hz, $A = 0.0496\lambda_0$; (*b*) and (*d*) ——— $f = 1.42$ Hz, $A = 0.0487\lambda_0$; · — · — · — $f = 1.42$ Hz, $A = 0.0496\lambda_0$; · · · — · · · — $f = 1.42$ Hz, $A = 0.0505\lambda_0$.

$f = 1.42$ Hz. The weakest breakers at each frequency were chosen for comparison rather than the breakers with equal values of A/λ_0 because various aspects of the data were in better agreement. The comparisons for other cases not shown herein can be extrapolated from the comparisons that are shown. In the following, some quantities are plotted dimensionally and others non-dimensionally, in order to better illustrate various findings.

Plots of the dimensionless crest height, y_m/λ_0, and the toe height, y_t/λ_0, versus X_{wm}/λ_0 are given in figure 19. The two plots on the left contain curves for the weakest breakers at each of the three frequencies while the two on the right contain curves for waves of different strength at $f_0 = 1.42$ Hz. This pattern of experimental conditions for the plots in this figure is repeated in all subsequent figures unless otherwise specified. For clarity of presentation, lines representing averages of the data for each experimental condition are shown rather than the individual data points. The comparisons of y_m/λ_0 in figure 19(*a*) indicate that the maximum wave height scales fairly well with λ_0. The maximum value for the case with $f_0 = 1.42$ Hz (0.0691) is about 2% higher than the maximum values for the other two frequencies (0.0683, 0.0677 for $f_0 = 1.26$ and 1.15, respectively). This trend is opposite to that for the values of

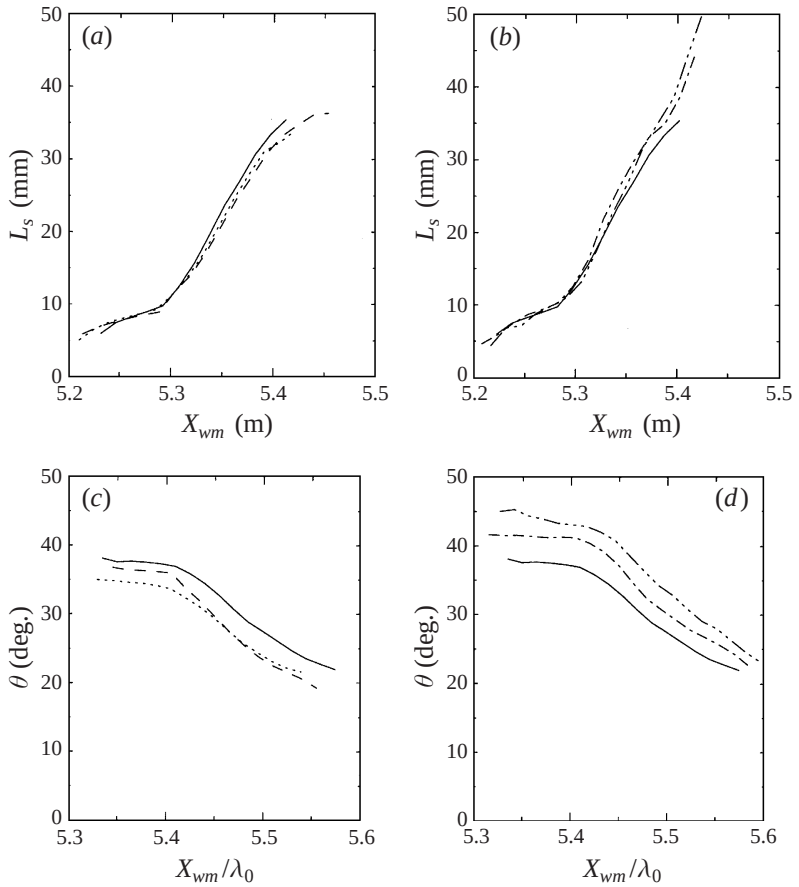

FIGURE 20. Bulge length (L_s), (*a,b*), and surface slope upstream of toe (θ), (*c,d*), versus distance from the wavemaker: (*a*) and (*c*) ——— $f = 1.42$ Hz, $A = 0.0487\lambda_0$; – – – – $f = 1.26$ Hz, $A = 0.0492\lambda_0$; ····· $f = 1.15$ Hz, $A = 0.0496\lambda_0$; (*b*) and (*d*) ——— $f = 1.42$ Hz, $A = 0.0487\lambda_0$; ·—·—·— $f = 1.42$ Hz, $A = 0.0496\lambda_0$; ···—···— $f = 1.42$ Hz, $A = 0.0505\lambda_0$.

A/λ_0 needed to produce these weakest breaking waves, see table 1. The differences in maximum height for the comparison of the waves with the same frequency but three different wavemaker amplitudes in figure 19(*b*) show similar differences in magnitude. The dimensionless wave height increases from 0.070 to 0.072 (2.9%) as A/λ_0 increases from 0.0487 to 0.0505 (3.7%).

The plots of the dimensionless toe height in figures 19(*c,d*) show a rather interesting result. Both the initial nearly constant values of y_t/λ_0 and the behaviour of y_t/λ_0 when the toe moves down the wave face are nearly the same for all waves. In fact, the initial value of y_t/λ_0 is less variable between experimental conditions than is the maximum value of y_m/λ_0. Just after the toe motion starts ($5.42 \leqslant X_{wm}/\lambda_0 \leqslant 5.47$) the data seem to follow a straight line, $\mathrm{d}y_t/\mathrm{d}X_{wm} \approx 0.135$, for all experimental conditions. Thus, changing variables from X_{wm} to time, it is found that $\mathrm{d}y_t/\mathrm{d}t \approx 0.135U$, where U is the carriage speed needed to move with the wave crest, see table 1.

Plots of L_s, the length of the bulge following the tangent to the surface just upstream of the toe, versus X_{wm} are given in figure 20(*a,b*). Note that L_s is plotted in millimetres and X_{wm} is given in metres. The waves of different frequencies break at very different locations in the tank. Thus, in order to better compare the data, the

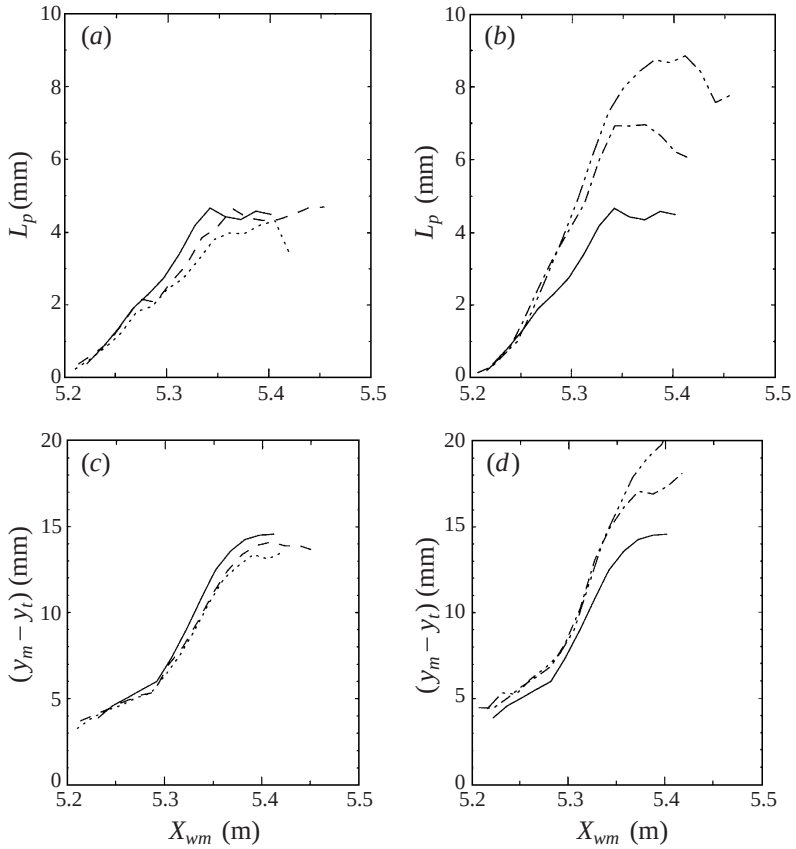

FIGURE 21. Bulge thickness (L_p), (*a,b*), and bulge height ($y_m - y_t$), (*c,d*), versus distance (X_{wm}/λ_0) from the wavemaker: (*a*) and (*c*) ——— $f = 1.42$ Hz, $A = 0.0487\lambda_0$; – – – – $f = 1.26$ Hz, $A = 0.0492\lambda_0$; ····· $f = 1.15$ Hz, $A = 0.0496\lambda_0$; (*b*) and (*d*) ——— $f = 1.42$ Hz, $A = 0.0487\lambda_0$; ·—·—·— $f = 1.42$ Hz, $A = 0.0496\lambda_0$; · · ·—· · ·— $f = 1.42$ Hz, $A = 0.0505\lambda_0$.

actual values of X_{wm} for the waves with frequencies of 1.15 and 1.42 Hz in figure 20(*a*) were shifted horizontally in the plots by −1.1 and 1.095 m, respectively. Note that when plotted dimensionally the curves are nearly identical in both plots. This means that in all cases, L_s starts with the same value and increases to the same value before the toe motion begins. The rate of increase of L_s both before and during toe motion scales with the wave phase speed. During toe motion, it is found that $\mathrm{d}L_s/\mathrm{d}t \approx 0.25U$.

Plots of θ, the angle of the tangent to the surface just upstream of the toe, versus X_{wm}/λ_0 are given in figures 20(*c,d*). The initial values for the three weakest breakers with different frequencies differ by about 3° but there is no consistent trend with increasing frequency. This lack of trend may be caused by errors in measuring the angle from the images. Indeed, comparisons of individual wave profiles, see §5, indicate that the slope of the surface for these three waves is nearly the same. For the cases with $f_0 = 1.42$ Hz, there is a definite increase in the initial θ with breaker strength. The rate of decrease of θ after the toe motion begins is fairly similar in all cases.

The thickness of the bulge, L_p, in mm is plotted versus X_{wm} in m in figure 21(*a,b*). For the three weakest breakers with the different frequencies, the data are very similar, particularly at smaller values of X_{wm}. Before the toe motion begins, the growth rate is linear and all three experimental conditions have nearly the same slope. After

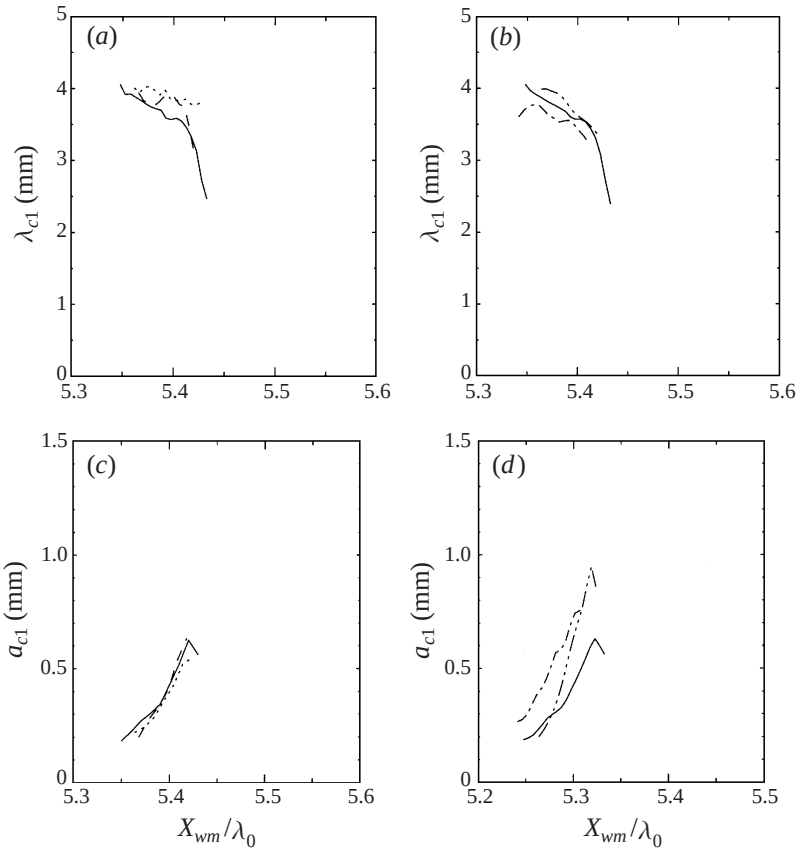

FIGURE 22. Capillary wavelength (λ_{c1}), (*a,b*) and capillary wave height (a_{c1}), (*c,d*), versus distance (X_{wm}/λ_0) from the wavemaker: (*a*) and (*c*) ——— $f = 1.42$ Hz, $A = 0.0487\lambda_0$; – – – – $f = 1.26$ Hz, $A = 0.0492\lambda_0$; · · · · · $f = 1.15$ Hz, $A = 0.0496\lambda_0$; (*b*) and (*d*) ——— $f = 1.42$ Hz, $A = 0.0487\lambda_0$; · — · — · — $f = 1.42$ Hz, $A = 0.0496\lambda_0$; · · · — · · · — $f = 1.42$ Hz, $A = 0.0505\lambda_0$.

this point the curves separate slightly. At roughly $X_{wm} = 5.33$ m, L_p becomes fairly constant at a value of about 4 mm. For the three waves with different wavemaker amplitudes at the same frequency, the stronger breakers reach larger values of L_p. This is one of the main effects of wavemaker amplitude on the geometrical characteristics measured herein. The maximum value of L_p increases from 4 mm to about 9 mm from the smallest to the largest values of A/λ_0, which differ by only about 3.7%.

In figure 21(*c,d*) the difference between the height of the crest and the height of the toe ($y_m - y_t$) is plotted in mm against X_{wm} in m. In all cases, the height difference increases linearly initially. This increase is due to a combined effect of the toe height decreasing (see figures 19*c,d*) and the crest height increasing (see figures 19*a,b*) during this phase of the motion. After the toe begins to move, $y_m - y_t$ at first increases more rapidly in a linear fashion and then slows down. The rapid increase in $y_m - y_t$ is primarily due to a rapid decrease in y_t. The curves for the weakest breakers at the three frequencies are quite similar, as are those for the two stronger breakers at $f_0 = 1.42$ Hz. However, these latter two curves are shifted above the curve for the weakest breaker at $f_0 = 1.42$ Hz.

Figure 22 contains plots of the wavelength (*a,b*) and amplitude (*c,d*) of the first capillary wave ahead of the toe for the five experimental conditions under consid-

eration. The total range of initial capillary wavelengths is only from 3.7 to 4.0 mm. In all cases, after the initial detection, the amplitudes of the capillary waves increase while the wavelengths decrease. The data here show more scatter than the previous measurements. However, it can be seen that for the three weakest breakers, the behaviour of the length of the first capillary wave is quite similar and the behaviour of the amplitude is almost identical. In comparing the results for the three waves with different strengths at $f_0 = 1.42$, it is found that the wavelength data are again quite similar while the amplitude data have significant differences.

5. Discussion

As was explained in §2.2, the experiments at the three different frequencies were performed in a Froude-scaled manner. Thus, when measured lengths are scaled by λ_0 and time by $1/f_0$, differences between waves generated at the same A/λ_0 but different frequencies can be attributed to the effects of surface tension and viscosity. The ratio of inertia effects to surface tension effects is measured by the Weber number, We, of the experiment,

$$We = \frac{\lambda_0^3 f_0^2}{\gamma}. \tag{5.1}$$

Since in these Froude-scaled experiments $\lambda_0 \propto f_0^{-2}$, the Weber number varies as f_0^{-4} and it increases by a factor of 2.3 from the highest to the lowest frequencies used herein. The ratio of inertia effects to viscous effects is measured by the Reynolds number, Re,

$$Re = \frac{\lambda_0^2 f_0}{\nu}, \tag{5.2}$$

where ν is the kinematic viscosity. The Reynolds number varies as f_0^{-3} and it increases by a factor of 1.9 from the highest to the lowest frequencies. Thus, it is expected that both surface tension and viscosity will play a significantly stronger role in the higher frequency, shorter waves. It should be emphasized that surface tension and viscous effects, while probably most important during the breaking process, also can affect the waves as they are generated and while they propagate from the wavemaker to the breaking location.

An important aspect of the flow is the evolution of the crest shape before the toe motion begins. During this part of the wave evolution, the flow is probably laminar and therefore more amenable to analysis than the later turbulent flow. In order to emphasize the data presented in the previous section (see figures 19–22) on the similarities and differences of the profiles of the crest before the toe motion begins, figures 23 and 24 are presented. Figure 23 shows a profile of the weakest breaker at each frequency. The profiles of the two waves with the lower frequencies were moved down vertically to make the crest heights equal for all three waves. All three profiles were taken from images that are within five frames ($\approx$ 10 ms) before the time when the toe begins to move down the wave face. (Exact comparisons of geometrical parameters should be taken from figures 19–22.) As can be seen from the figure and as was shown by the plots in the previous section, the three wave profiles are nearly identical in spite of the fact that the wavelength of the lowest frequency wave is about 1.5 times that of the highest frequency wave. This similarity includes the lengths of the capillary waves and the bulge as well as the surface shape upstream of the toe and downstream of the crest. In figure 24, profiles at similar times in the evolutions of three waves with $f_0 = 1.42$ Hz but three values of A/λ_0 are presented.

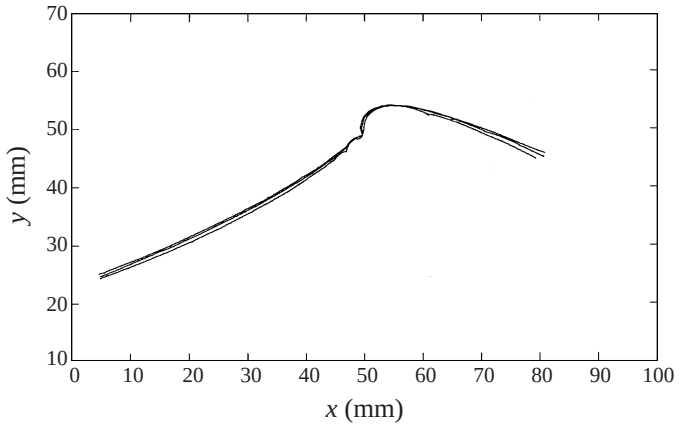

FIGURE 23. Crest profiles at similar stages before toe movement for the weakest breakers at three frequencies: $f = 1.42$ Hz, $A/\lambda_0 = 0.0487$; $f = 1.26$ Hz, $A/\lambda_0 = 0.0492$; $f = 1.15$ Hz, $A/\lambda_0 = 0.0496$. The profiles of the two lower frequency waves have been moved vertically so that the crest heights are equal.

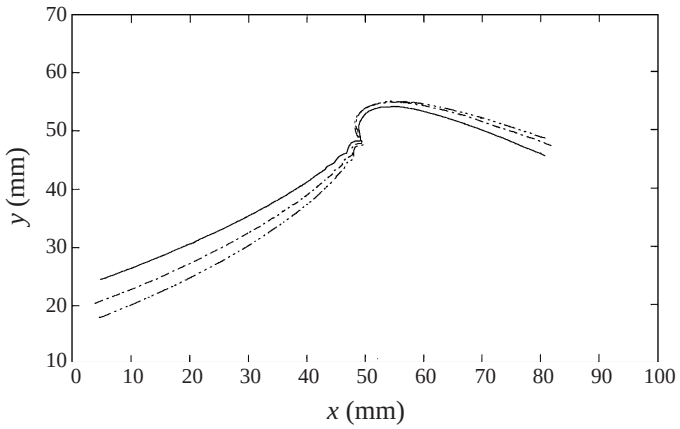

FIGURE 24. Crest profiles at similar stages before toe movement for $f = 1.42$ Hz with three breaker strengths: ——— $A = 0.0487\lambda_0$; · — · — · — $A = 0.0496\lambda_0$; · · · — · · · — $A = 0.0505\lambda_0$.

No vertical shifting was performed in plotting these profiles. As can be seen from the figure, the toe heights and the lengths of the bulge and the capillary waves are the same and there is a slight variation in crest height. However, there is a larger variation in the slope of the front and rear wave faces with steeper front face slopes and less steep rear face slopes corresponding to higher A/λ_0. As can be seen from figure 20, the front face steepness (θ) is nearly independent of time in the beginning of the breaking process so the variation in θ depicted in figure 24 is independent of the particular frames that were chosen in each image sequence for the comparison. As can be deduced by noting the variations in the wave shape in figure 24, the excellent overall agreement in wave shape found in figure 23 would not be as good if waves at the three frequencies with the same A/λ_0 had been compared instead of comparing the weakest breakers at each frequency.

The similarities in the wave shape, illustrated by figures 23 and 24 emphasize the findings of the previous section: the height of the toe scales with λ_0, the height of the

crest nearly scales with λ_0, the slope of the front face upstream of the toe increases with increasing A/λ_0 and the remainder of the shape parameters describing the crest are independent of λ_0 and A/λ_0 for $77 \leqslant \lambda_0 \leqslant 118$ (the range of λ_0 investigated in this experiment). Thus, the wave height, toe height and front face steepness scale with outer wave characteristics (g and f_0 or λ_0) while the shapes of the capillary waves and the bulge do not. The lack of variation of the crest features implies, assuming that viscous and surfactant effects are not important, that the length scale, ℓ_c, for flow in the crest is a function only of gravity, g, and surface tension, $\gamma = T/\rho$ (where for pure water $T \approx 72$ dyne cm^{-1}); therefore,

$$\ell_c = (\gamma/g)^{1/2}. \tag{5.3}$$

This length scale applies to the bulge as well as the capillary waves upstream of the toe. At the instant before the toe motion begins, there is little variation in the length of the first capillary wave and the length of the bulge from one experimental condition to another. Typical values are

$$\lambda_{c1} = 1.3\ell_c, \quad L_s = 3.69\ell_c. \tag{5.4}$$

At the same point in the wave evolution, the variation of the heights of the first capillary wave and the bulge from one experimental condition to another is larger than the variation of their lengths but typical values are

$$a_{c1} = 0.18\ell_c, \quad L_p = 1.1\ell_c. \tag{5.5}$$

It would be interesting to make quantitative comparisons of the experimental data presented on the crest profiles before the toe motion begins with the existing theoretical analyses mentioned in the §1. However, it should be pointed out that the assumptions of the theories and the details of the experiments are at odds in some respects. Most importantly, the theories invariably assume some type of perturbation of a steady flow, while in the experiments the wave crest goes through large changes in shape in time intervals that are less than one wave period. Another problem is that the theories usually assume that the basic wave profile is symmetric about the crest while the experimental wave crests are highly asymmetric. For these reasons quantitative comparisons with the theories are difficult. The following discussion points out the qualitative similarities and differences between the theory and the experiments as well as the difficulties in making quantitative comparisons.

The initial formation of the bulge and toe are qualitatively similar to the theoretical predictions of Longuet-Higgins & Cleaver (1994), Longuet-Higgins *et al.* (1994), and Longuet-Higgins & Dommermuth (1997). However, the theory is based on potential flow with no surface tension, while the present results indicate that the length scales of the crest shape are given by ℓ_c. Thus, it is unlikely that quantitative agreement with the theory would be possible. If one were to proceed with the comparison in spite of this problem, one might try to compare the theory's prediction on the position of the toe relative to the crest and the growth rate of the bulge as described in the introduction of the present paper. These quantitative comparisons require a measurement of R, the radius of curvature of the crest before the appearance of the bulge. Unfortunately, in the experiments the crest profile is changing rapidly before the first appearance of the bulge (see the profile history in figure 14) and no single value of R can be determined.

The shape of the bulge and the capillary waves upstream of the toe are also quite similar to that predicted by the capillary jump theory of Longuet-Higgins (1996*b*). This theory is based on capillary–gravity solitary waves and again assumes a steady

wave profile upon which the jump is added at the location with the proper local surface flow speed. The leaky jump shown in figure 5(*b*) of that paper most closely matches qualitatively the surface shapes found in the present experiments. Critical to the theory is the requirement that at the location of the jump $q < c'_{min}$, where q is the surface flow speed and $c'_{min} = (4g'\gamma)^{1/4}$, where g' is the local apparent gravity given by $g' = g\cos\alpha - \kappa q^2$, where α is the angle of tilt of the surface and κ is the local curvature. Since the present flow is unsteady, it is not possible to accurately calculate the local flow speed near the location of the toe from the steady Bernoulli equation, thus quantitative comparisons are not possible. If one were to ignore the unsteady aspect of the flow, the fact that the initial dimensionless toe height, y_t/λ_0, is the same for all waves measured herein would indicate from the steady Bernoulli equation that the flow velocity at the surface at the position of the toe would vary in proportion to the wave phase speed. Thus, the capillary jump would occur in regions of different flow velocity for the various wave frequencies. However, this difficulty probably only points out that unsteady theory is required to achieve quantitative agreement with the experiments.

Direct numerical simulations of gentle spilling breakers with variable surface tension were presented by Yao *et al.* (1996). Some of these results are also presented in Longuet-Higgins (1996*b*). These simulations use a boundary element code which models the wave tank and wavemaker. The wavemaker motion and other experimental conditions used in the present experiments were also used in the numerical calculations, but the effective surface tension was varied. The resulting crest profiles are quite similar to those measured in the present experiments. It is pointed out in Longuet-Higgins (1996*b*) from Yao *et al.*'s calculations with surface tensions of 9 and 16 times that of pure water that the crest structure when non-dimensionalized by ℓ_c is the same for both waves. The present experimental results essentially show the same result by keeping the surface tension constant and varying the frequency with Froude-scaled generation conditions.

It is also tempting to compare the findings on the capillary waves upstream of the toe in the experiments to theoretical results. One steady flow idea would be to assume that the wavelength of the capillary waves upstream of the toe is determined by the condition that in order for these waves to be steady relative to the wave crest, the underling flow speed must equal the capillary wave phase speed. Unfortunately, this appealing idea is apparently not applicable since the toe position, which is at approximately the location of the first capillary wave, scales with λ_0 while the capillary wavelength is independent of λ_0. From the first result, steady theory implies that the velocity at the location of the toe is given by

$$u_t = c_0\left(1 - \frac{4\pi y_t}{\lambda_0}\right)^{1/2}, \tag{5.6}$$

where $c_0 = (g\lambda_0/(2\pi))^{1/2}$. Since y_t/λ_0 is constant for all experimental conditions, the above equation implies that u_t varies as c_0. For pure capillary waves, from linear theory

$$\lambda = 2\pi\gamma/c^2, \tag{5.7}$$

where c is the phase speed of the capillary wave. So, with c replaced by u_t in the above equation, according to these steady flow ideas one would expect the capillary wavelength to decrease by a factor of 1.5 from $f_0 = 1.42$ Hz to $f_0 = 1.15$ Hz. The variations found in the data, see figure 22, are much smaller than this value. This lack of agreement is probably again just a reflection of the inadequacy of the steady theory when applied to these unsteady waves.

After toe motion begins, the flow appears to be turbulent. The toe velocity, as measured by either $\mathrm{d}y_t/\mathrm{d}t$ or $\mathrm{d}L_s/\mathrm{d}t$, quickly accelerates to a constant velocity which is proportional to the wave crest speed. Thus, the motion of the toe scales with the outer wave characteristics.

6. Conclusions

Measurements of the crest profile history of gentle spilling breakers generated mechanically with a dispersive focusing technique were presented. The wave generation parameters were Froude scaled with three average wave packet frequencies, $f_0 = 1.42$, 1.26 and 1.15 Hz, and different overall wavemaker amplitudes at each frequency. Surfactant levels in the wave tank were kept low by continuous skimming and the surface tension was monitored using an *in situ* Langmuir trough with a Whilhelmy plate. It was found that all of the waves broke without the overturning of the water surface that is characteristic of plunging breakers. Instead, the breaking process began with the formation of a bulge near the crest on the forward face of the wave and capillary waves formed upstream of the leading edge or toe of the bulge. The shape and lengths of these features were found to be nearly independent of wave frequency and wavemaker amplitude which lead to the conclusion that the length scale for these surface features was $\ell_c = (\gamma/g)^{1/2}$, where $\gamma = T/\rho$ and T and ρ are the surface tension and density of water, respectively. The toe remained fairly stationary relative to the wave crest during the formation of the bulge but soon began to move down the front face of the wave. Ripples were generated between the toe and the crest during this phase of the breaking process. These ripples initially moved at the same speed as the wave crest; however, as the breaking process continued, their speed decreased. The initial height of the toe was approximately $0.062 \pm 0.001\lambda_0$ (where $\lambda_0 = g/(2\pi f_0^2)$) in all cases and the vertical velocity of the toe as it moved down the wave face was about $0.135U$ where U is the horizontal speed of the wave crest. Thus, the initial toe height and its subsequent vertical velocity scale with the outer variables that describe the overall wave rather than with ℓ_c. The main effects induced by increases in A/λ_0 for any one frequency were an increase in the surface slope upstream of the toe, a decrease in the surface slope downstream of the crest, and an increase in the maximum thickness of the bulge. It is emphasized that the details of the shape of the crest and the range of gravity wavelengths over which the above described phenomena occur may change for breakers generated with different wavemaker motions or in the presence of wind or surfactants.

The support of the Office of Naval Research under contracts N000149610368, Program Officer Dr Edwin P. Rood, and N000149610474, Program Officer Dr Dennis Trizna, is gratefully acknowledged. The authors would also like to express their gratitude to M. S. Longuet-Higgins for a number of helpful discussions, to J. Milgram and W. Barger for suggestions of methods to measure the surface tension, and to H. Parkhurst who performed some of the processing of the images to determine the capillary wavelengths and amplitudes.

REFERENCES

Amini, A. A., Weymouth, T. E. & Jain, R. 1990 Using Dynamic Programming for solving variational problems in vision. *IEEE Trans. PAMI* **12**, 855–867.

Barr, A. 1984 Global and local deformations of solid primitives. *Comput. Graphics* **18**, 21–30.

Blake, A., Curwen, R. & Zisserman, A. 1993 A framework for spatiotemporal control in the tracking of visual contours. *Int. J. Computer Vision* **11**, 127–145.

Bonmarin, P. 1989 Geometric properties of deep-water breakng waves. *J. Fluid Mech.* **209**, 405–433.

Brown, C. M. 1983 Inherent bias and noise in the hough transform. *IEEE Trans. PAMI* **5**, 493–505.

Chakraborty, A., Worring, M. & Duncan, J. S. 1995 On multi-feature integration for deformable boundary finding. *Proc. ICCV*, pp. 846–851.

Crapper, G. D. 1957 An exact solution for progressive capillary waves of arbitrary amplitude. *J. Fluid Mech.* **2**, 532–540.

Delagnes, P., Benois, J. & Barba, D. 1995 Active contours approach to object tracking in images sequences with complex background. *Pattern Recognition Lett.* **16**, 171–178.

Duda, R. O. & Hart, P. E. 1975 Use of the Hough transform to detect lines and curves in pictures. *Commun. As. Comput. Mach.* **15**, 11–15.

Duncan, J. H., Qiao, H., Behres, M. & Kimmel, J. 1994*a* The formation of a spilling breaker. *Phys. Fluids* **6**, 2558–2560.

Duncan, J. H., Philomin, V., Qiao, H. & Kimmel, J. 1994*b* The formation of a spilling breaker. *Phys. Fluids* **6**, S2.

Ebuchi, N., Kawamura, H. & Toba, Y. 1987 Fine structure of laboratory wind-wave surfaces studied using an optical method. *Boundary-Layer Met.* **39**, 133–151.

Foley, J. D., Van Dam, A., Feiner, S. K. & Hughes, J. F. 1993 *Computer Graphics, Principle and Practice.* 2nd Edn. Addison-Wesley.

Harwood, D., Subbarao, M., Hakalahti, H. & Davis, L. S. 1984 A new class of edge-preserving smoothing filters. *CAR-TR-59, Center for Automation Research, University of Maryland.*

Illingworth, J. & Kittler, J. 1987 The adaptive Hough transform. *IEEE Trans. PAMI* **9**, 690–698.

Lai, K. F. & Chin, R. T. 1994 Deformable contours: modeling and extraction. *Proc. IEEE Computer Vision and Pattern Recognition*, pp. 601–608.

Longuet-Higgins, M. S. 1975 Integral properties of periodic gravity waves of finite amplitude. *Proc. R. Soc. Lond.* A **342**, 157–174.

Longuet-Higgins, M. S. 1992 Capillary rollers and bores. *J. Fluid Mech.* **240**, 659–679.

Longuet-Higgins, M. S. 1994 Shear instability in spilling breakers. *Proc. R. Soc. Lond.* A **446**, 399–409.

Longuet-Higgins, M. S. 1996*a* Progress towards understanding how waves break. Presented at *21st Symposium on Naval Hydrodynamics, Trondheim, Norway, June 24–28.*

Longuet-Higgins, M. S. 1996*b* Capillary jumps on deep water. *J. Phys. Oceanogr.* **96**, 1957–1965.

Longuet-Higgins, M. S. & Cleaver, R. P. 1994 Crest instabilities of gravity waves. Part 1. The almost-highest wave. *J. Fluid Mech.* **258**, 115–129.

Longuet-Higgins, M. S., Cleaver, R. P. & Fox, M. J. H. 1994 Crest instabilities of gravity waves. Part 2. *J. Fluid Mech*, **259**, 333–344.

Longuet-Higgins, M. S. & Dommermuth, D. G. 1997 Crest instabilities of gravity waves. Part 3. Nonlinear development and breaking. *J. Fluid Mech.* **336**, 33–50.

Okuda, K. 1982 Internal flow structure of short wind waves Part I. On the internal vorticity structure, *J. Oceanogr. Soc. Japan* **38**, 28–42.

Rapp, R. & Melville, W. K. 1990 Laboratory measurements of deep water breaking waves. *Phil. Trans. R. Soc. Lond.* A **331**, 735.

Rosenfeld, A. & Kak, A. 1982 *Digital Picture Processing*, Academic.

Schooley, A. H. 1958 Prifles of wind-created water waves in the capillary-gravity transition region. *J. Mar. Res.* **16**, 100–108.

Tulin, M. P. 1996 Breaking of ocean waves and downshifting. In *Waves and Nonlinear Processes in Hydrodynamics*, pp. 177–190. Kluwer.

Yao, Y., Wang, P. & Tulin, M. P. 1996 Surface tension effects on breaking waves—LONGTANK simulation. *Tech. Rep.* 95-132. University of California, Santa Barbara.